Stony Brook University

Development of the Spatially-Resolved Laser Flash Thermal Conductivity Instrument

A Thesis Presented

by

Rodney Yeung Vee Kao

to

The Graduate School

in Partial Fulfillment of the

Requirements

for the Degree of

Master of Science

In

Mechanical Engineering

(Thermal Sciences and Fluid Mechanics)

Stony Brook University

August 2008

Stony Brook University

The Graduate School

Rodney Yeung Vee Kao

We, the thesis committee for the above candidate for the

Master of Science degree, hereby recommend

acceptance of this thesis.

Jon Longtin – Thesis Advisor
Associate Professor – Mechanical Engineering

Lin-Shu Wang – Chairperson of Defense
Associate Professor – Mechanical Engineering

Thomas Cubaud – Committee Member
Associate Professor – Mechanical Engineering

This thesis is accepted by the Graduate School

Lawrence Martin
Dean of the Graduate School

Abstract of the Thesis

Development of the Spatially-Resolved Laser Flash Thermal Conductivity Instrument

by

Rodney Yeung Vee Kao

Master of Science

in

Mechanical Engineering

(Thermal Sciences and Fluid Mechanics)

Stony Brook University

2008

The thermal conductivity and thermal diffusivity of solids are the most important thermophysical material parameters for describing the heat transport properties of a material or component. The thermal conductivity and diffusivity is used for both technological and scientific purposes, especially in heat transfer and thermal processing. This work introduces a spatially-resolved laser flash thermal concept to measure the thermal conductivity and thermal diffusivity of an ultra-thin silicon wafer. The key methodology in the experiment is the use of an improved temperature-sensing technique

based on thermoreflectance of a CW He-Ne probe laser to detect the temperature history on the backside of the sample. A very stabilized pulsed Nd:YLF based laser system is used as the heating source. A heating pulse from the laser is thus generated resulting in a time-dependant temperature rise, caused by the change in refractive index of the wafer. A numerical simulation analysis of the transient heat conduction, together with the probe beam reflectivity models and experimental results, are used to determine the thermal conductivity and diffusivity of the silicon wafer. The experiment used is small, cheap and reliable. Some improvements in the optical set-up and equipments can better the results obtained.

Table of Contents

List of Figures

List of Tables

Nomenclature

A	surface area [m^2]
C_p	specific heat [J/kg*K]
d	heating laser diameter [mm]
E_p	heating pulse energy [mJ]
f	lens focal length [mm] (Chapter 4,5), frequency [KHz] (Chapter 5)
G	Gain-Amplifier [V/nA]
I	laser beam intensity [μW]
i	photocurrent, [nA]
k	thermal conductivity [W/m*K] (Chapter 3,5) , extinction coefficient [ ] (Chapter 3,4)
n	index of refraction [ ]
q''	laser heat flux [W/m^2]
P	experimental reflectivity [ ] (Chapter 4), Power [W] (Chapter 4)
R	radius of heating laser beam [mm] (Chapter 3), responsivity of photodiode [A/W] (Chapter 4)
R_w	radius of wafer [mm]
T, T_∞	temperature, ambient temperature [ºC]
t	time [s]
$t_{1/2}$	rising half-time [ns]
U	Uncertainty [ ]
V	voltage [V]

Greek Symbols

α	thermal diffusivity [m^2/s]
λ	wavelength [nm]
ρ	density [kg/m^3] (Chapter 3) , probe beam reflectivity [ ] (Chapter 3 and 4)
θ	angle of incidence [º]
τ	pulse duration [ns]
$\tau_{1/2}$	generalized half-time dimensionless coefficient [ ]
ϕ	azimuthal angle [rad]
$\frac{dk}{dT}$	change in extinction coefficient with time [1/ºC]
$\frac{dn}{dT}$	change in index of refraction with time [1/ ºC]
$\frac{d\rho}{dT}$	change in reflectivity with time [1/ ºC]

Subscript

0	initial condition
1,2	medium 1,2
I	incident
p	pulse, p-polarization plane
R	reflected
s	s-polarization plane
w	wafer

Acknowledgements

I am very thankful to my advisor, Professor Jon Longtin for his guidance, help and advice throughout my graduate and undergraduate career. Prof. Longtin has also offered me academic and financial supports that helped me to successfully complete my Masters thesis. As his graduate and research student, I have learnt a tremendous amount under his supervision. His seriousness, assiduity and strictness with scientific and experimental research make him a lead example for students to follow.

I would like to thank Professor Thomas Cubaud for his contributions and advice to my work. Professor Cubaud kindly offered me suggestions in my experiments and allowed me to use of some of his ultra-thin wafers.

I would like to show my appreciation to Professor Lin-Shu Wang, who accepted to be the chair of my thesis committee.

Some acknowledgements go to my fellow graduate and past undergraduate students for their contributions to my work. Ms Cristina Catero contributed in the reflectivity model during the summer of 2006, while Mr Yang Tan assisted in the simulation model and some other useful suggestions to the present work. Mr Chang Tang also helped in machining some of the parts used in my optical system.

Finally, I thank my parents and relatives for their everlasting support throughout my college and graduate career. Their encouragement and support inspired me to succeed in my studies.

1. Introduction

The thermal conductivity and thermal diffusivity are two very important thermal properties in the field of heat transfer. Their accurate values are essential in design engineering as well as in theoretical studies. Both the thermal conductivity and diffusivity characterize the heat transfer behavior of solids, conduction and convection heat transfer applications, heat exchange designs and insulation analysis. With the use of different numerical simulation techniques, the properties can describe the temperature distribution along any solid of different material in a steady but also in a transient state. The availability of those two parameters is heavily depended on in the heat transfer field.

1.1 Experimental Background

Several techniques have been developed over the years to measure thermal conductivity of solid materials. These techniques depend on factors such as material, form (bulk sample, coatings-thin and -thick, etc), temperature range, thermal conductivity range and required measurement precision. These techniques, however, have benefits and drawbacks.

The measurement of thermal conductivity and thermal diffusivity could be classified into two categories: steady-state and unsteady-state. For steady-state method, a macroscopic steady temperature gradient of the sample is required to be established first before any measurement is initiated. Therefore the run time is comparatively long.

However, measuring diffusivity requires an accurate recording of the time dependence of temperature following a transient, or periodic, temperature perturbation at a specimen boundary. For diffusivity measurement, transient methods are usually preferred.

Some examples of steady-state method include the Comparative Method [1,2] where a test specimen is sandwiched under load between two reference materials, each in contact with the flat plate of a heating/cooling unit, and the whole stack is surrounded by a longitudinal guard cylinder. A temperature gradient is established along the stack and longitudinal heat flow assured by matching the temperature gradient in the guard to that in the specimen stack. Thermal conductivity is derived from measurements of the temperature differences across the reference and test specimens. Comparative method works for all solids with measurements over a temperature range of 100-1300K, but definitive attachment of temperature sensors at required positions to test and reference pieces are critical. Care should be taken to eliminate, or maintain, reproducible contact resistances at mating surfaces.

The Four Probe technique [3-5] measures thermal conductivity via electric resistivity. A direct current is passed through a cylindrical sample and its electric resistivity is determined by measuring the voltage drop between two probes positioned at a fixed distance. All these values have to be measured with high accuracy. Setbacks include systematic errors arising from determination of the voltage drop because of thermoelectric voltage between the sample and the electrodes. This method generally tests metals and metallic alloys. Also, measurements of molten metal are much more difficult than measurements only on solids because the sample must be kept inside a ceramic tube. The sample shape and temperature are more difficult to determine in this

case and the complicated mechanics of the electrodes may lead to increased measurement errors. Thermal conductivity in this method is calculated using the Wiedemann-Franz law.

The Guarded Heat Flow method [6-8] utilizes a heat flux transducer together with reference materials as calibration artifacts. However, it is specifically designed for measuring specimens having thermal resistances in the range 0.2-20 W/m*K, and in particular hard solids, using smaller test specimens in the range 30 mm to 50 mm diameter and 1 mm to 30 mm thick depending on the thermal conductivity. It can also be used to measure thin sheets (by stacking multiple sheets together), and highly viscous materials. Calibration must be undertaken under the same temperature and pressure conditions as those for the test specimen.

Some less common techniques such as Guarded Hot Plate [8-10] and Heat Flow [11-13] meter are similar to, or derived, from Guarded Heat Flow and Comparative method. They are mostly for insulating and low conductivity materials.

All these techniques, however, usually made direct use of the transport equations by measuring physical quantities such as heat flux and temperature gradients. These measurements are difficult to operate; heat losses at boundaries and convective or radiative effects in the sample are the main error sources.

For many years one contact transient technique, the Hot-wire method [14-18], has been used to measure the thermal conductivity, and in some forms the thermal diffusivity and specific heat of both solids (and fluids). This method uses a heating wire pressed directly between two specimen pieces as the power source and the thermal properties are obtained from the temperature-time response due to a heat flux generated by the wire. More recently a modification of the method called the ‘hot strip’ technique has also been

developed. Continuing improvements have been made in modeling of these techniques, design of apparatus and instrumentation hardware. As a result several new methods based on the same common principle as that used for the hot wire and hot strip have evolved. These methods either measure one or several thermophysical properties of high-density homogeneous solids - thermal conductivity, thermal diffusivity or in some forms thermal effusivity and specific heat. Different variants of this basic method also allow measurement of thin films, very good conductors in sheet form and also anisotropic materials. However some uncertainties and inter-related effects may be present due to the particular assumptions that are used in models.

Due to the ever increasing growth in materials development, especially in coatings, there has been a corresponding increased demand to develop new methods of measurement of thermal properties which are faster, use smaller more easily produced specimens, and measure multi-properties. Nowadays more emphasis is made on coatings and thick-film structures (10μm-1mm thick); as they represent an extremely important class of technologies that include thermal barrier coatings based on zirconia for thermal protection of turbine components [28-29], wear coatings [30-31], emerging MEMS and power-electronics applications, and coating used for sensor applications [32]. The thermal conductivity can be profoundly influenced by the internal structure of the coating, which in turn is dictated by the deposition process. This is used to advantage in thermal spray coatings, for example, that are used for thermal protection in aircraft components for enhanced thermal efficiency: the highly defective structure markedly reduces the coating thermal conductivity. Because the coating structure plays such a significant role in its thermal conductivity, one cannot use conventional bulk values of thermal

conductivity because it does not possess the final coating structure. As such a technique capable of measuring the thermal conductivity *in-situ* in an actual coating is critical. Accurate measurements of coating thermal conductivity and thermal diffusivity are complicated by the fact that the coatings are seldom uniform, homogenous, or fully dense. In addition, coatings and films are often highly anisotropic, and properties can vary as a function of in-plane position as well. Conductivity and diffusivity measurements for bulk materials are simply insufficient to characterize coatings or films to the level of sophistication required for modern coating design and application.

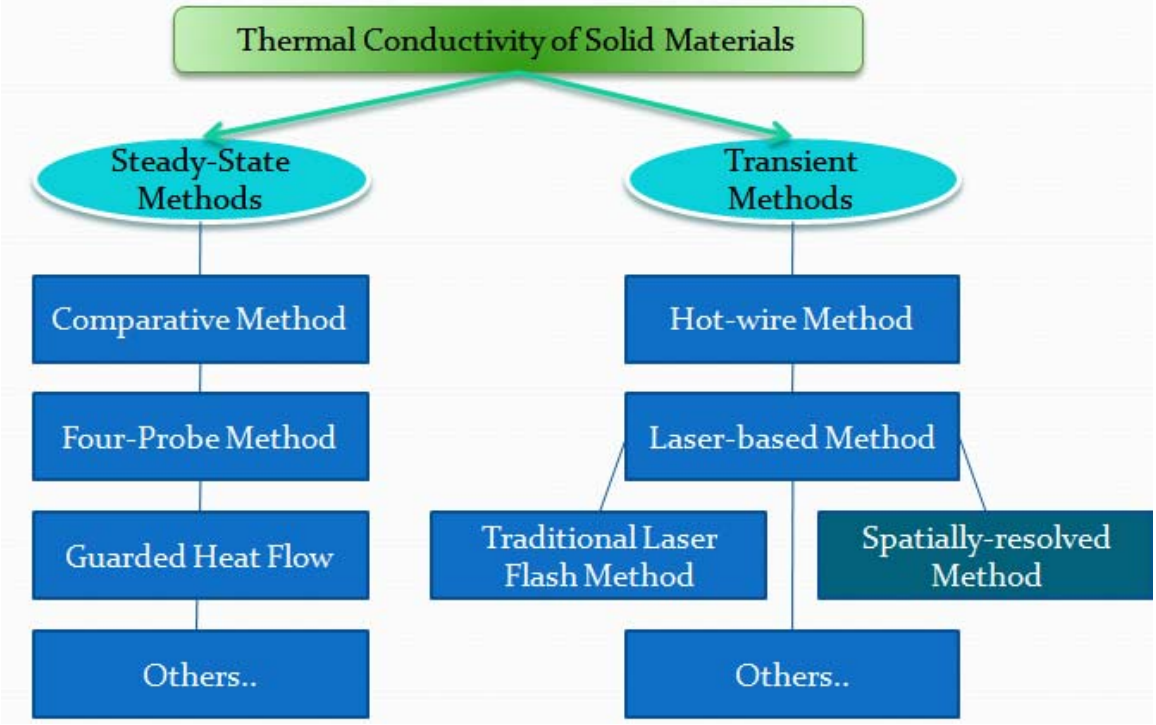

Figure 1: Several thermal conductivity measurement techniques for solid materials

Laser-based techniques, following the invention of the laser in 1960, became popular in numerous researches on solid thermophysical properties. Compared to conventional method, laser-based techniques are fast, easy to operate and have high sensitivity.

The flash technique [19-21] is the most frequently used technique to measure thermal diffusivity for moderate to good thermal conducting materials (≥ 0.5 W/m*K) in the perpendicular to surface direction. In-plane measurements can be made using modifications of the method involving a "point" energy source and radial temperature measurements across the back surface. The basic method is based on measurement of the temperature rise on the back face of a thin disc sample caused by a short energy pulse on the front surface. This method is one of the most popular techniques and refined by researchers over the years. It has since been refined subsequently by several groups over the years.

The traditional laser flash method, in Figure 2, is used to heat up the top surface of the coating. The time-varying temperature history at the bottom of the coating is recorded with an infrared (IR) detector, and the temperature history is correlated to the thermal diffusivity, α, of the coating. The technique measures the thermal diffusivity of the film α (m^2/s) and as $\alpha = (k/\rho C_p)$, the thermal conductivity k (W/m*K) can be determined provided the density ρ (kg/m^3) and the specific heat C_p (J/Kg*K) are known.

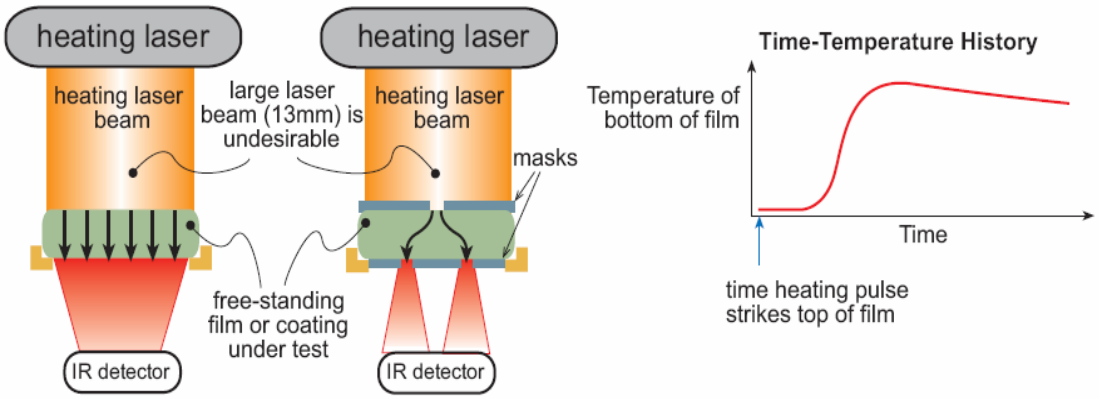

Figure 2: The traditional laser flash technique

However, there are some shortcomings associated with the traditional laser. The substrate must be manually removed from the coating prior to testing, which is labor intensive and prone to user-to-user variation. The reported thermal conductivity is an integrated value; the technique *cannot* resolve spatial variations in thermal properties within the test specimen. The sample must be fabricated to specific, exacting dimensions, e.g., a circular disk 12.7 mm in diameter and of constant thickness, which is done by hand, is time consuming, prone to error, and subject to the vagaries of the individual operator doing the processing. Small (<3 mm) and large (>25 mm) samples represent formidable challenges that often simply cannot be measured. The in-plane thermal conductivity measurement requires a different experimental configuration, and has a large uncertainty associated with it, as shown in the center of Figure 2. The time-response of the system is limited by the infrared detector, which makes fast detection (measurement of thin coatings) challenging and error prone. Transmission through the sample or refraction of the incident heating laser pulse can distort the measurement due to laser radiation entering the IR detector. Thermal radiation at high temperatures can complicate the IR detector signal.

The traditional laser flash technique has been used for over four decades and yet this is still much more room for improvement.

1.2 Concept of Thermoreflectance Technique

This work describes a high-precision thermal pulse method to measure the thermal conductivity of a thin silicon wafer using a laser based thermoreflectance technique in the

place of the traditional IR detector to measure the temperature variation at the back of the wafer and a focused laser beam to heat the wafer.

Referring to Figure 3, the technique involves a pulsed Nd:YLF laser (14~16mJ/pulse, 170-200ns pulse width) to irradiate a region on the top of the wafer. A CW He-Ne probe laser, with a diameter of 0.7139 mm at zero angle of incidence, is reflected off on the rear surface of the wafer. The time-dependent change in reflectivity of the probe beam is monitored and correlated to the interface temperature history which can be used to calculate the thermal diffusivity and conductivity.

In other words, as the wafer is heated, a temperature gradient is formed and thus causes a change in refractive index in the wafer. The CW He-Ne probe laser, in turn, is deflected due to the refractive index gradient in the wafer and the time varying temperature rise is recorded. A numerical analysis, which includes the thermal conductivity of the test wafer, is modeled on ANSYS. A comparison on the time-varying thermal profile from the numerical model can be made with that from the experiment so that the thermal conductivity and diffusivity in the model can be properly adjusted to yield the best agreement. Silicon wafer is used in this experiment because of its smoothness and flat surface. The optical properties of Silicon have been well studied, as its refractive and extinction coefficients, that depend on temperature, have been derived and can be easily found from literature.

There are several advantages of this technique. Firstly, the small spot size of the heating and temperature measurement lasers provide the ability to high resolution spatially-resolved thermal conductivity characterization. This provides the ability to measure thermal conductivity at a specific region in the film. Secondly, both through-

thickness and in-plane thermal conductivity can be measured with the same sample simultaneously. By orienting the laser directly above the temperature sensing laser spot, the through-thickness thermal conductivity can be measured, while an offset between the heating laser and the laser probe provides the in-plane conductivity measurements.

Table 1 summarizes the best features associated with the spatially-resolved concept and some shortcomings of the traditional laser flash method.

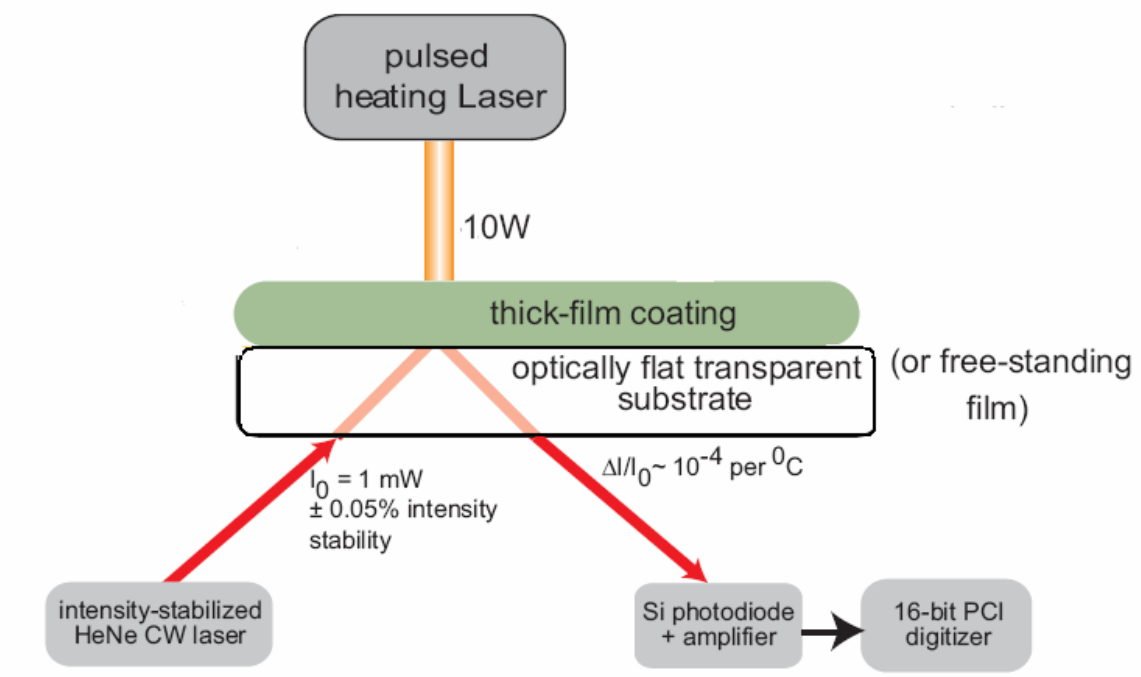

(a)

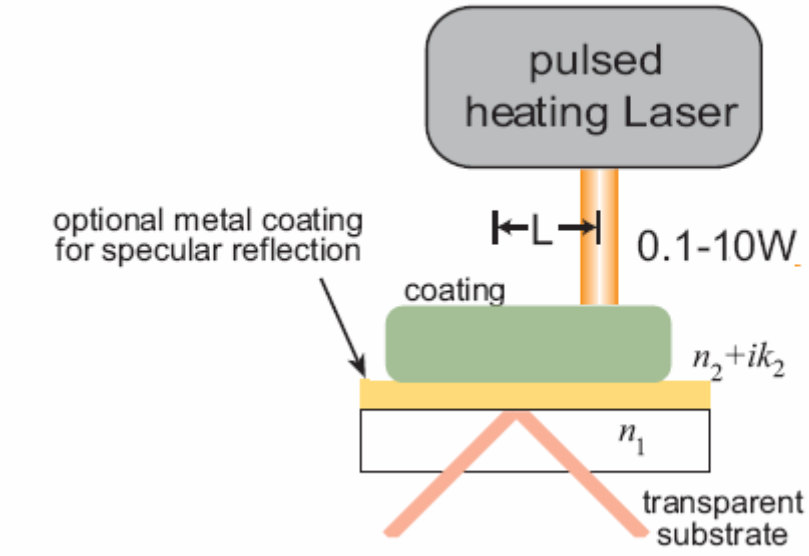

(b)

Figure 3: Schematic of the thermoreflectance technique: (a) through-plane and (b) in-plane measurements

Feature	Spatially-Resolved Laser Flash	Traditional Laser Flash
Substrate Removal	Not required	Required (labor intensive)
Spatial Resolution	High. A few μm expected	Very Low. About 1 cm
Temporal Resolution	High	Moderate (10–50 μs)–limits range of testable film thickness
High-Temperature Operation	Straightforward; signal not affected by radiation	Radiation at high temperature can saturate IR detector
Through-thickness and In-Plane Thermal Conductivity	Same setup	Requires different fixtures; in-plane measurements have considerable uncertainty
Sample Absorption	Heating laser pulse will not affect temperature measurement	Coating must absorb strongly; else IR detector will detect transmitted heating laser pulse
Sample Size Range	50 μm – 10+ cm large sample size range	1.3 cm (typical) sample size is fixed

Table 1: Comparison of Spatially-Resolved Laser Flash and Traditional Laser Flash Techniques for Thermal Property Measurement

1.3 Outline of Present Work

The experimental set-up and all the equipments used are described in details in Chapter 2. The set-up is custom-designed and built for this study. The advantages of this set-up are: its simplicity, very reliable and easy to operate. Discussions on the sample choice and instrument concept are also justified, with some preliminary results.

The physical models for both the heat conduction through the sample and the probe beam reflectivity change, caused by the heating laser, are discussed in Chapter 3. Some background theories of optics and plane polarizations, as well as the thermoreflectance models, are outlined in details. The later part of the chapter also includes a finite numerical simulation to solve the governing heat conduction equations and obtain the time-dependent temperature rise at the rear of the wafer.

In Chapter 4, validation of the final experiment is made by a series of experiments and analytical verifications. These include measuring the heating and probe beam diameters, the heating pulse duration and energy, and the silicon wafer thickness. A device to align the probe beam and the heating beam is also introduced.

Data collection and processing of the final experiment is described in Chapter 5. The initial results are obtained and modifications of the set-up leading to the thermal signal are discussed. The resulted time-dependent heat conduction profile is plotted with those predicted by the numerical model. Thus the thermal conductivity and thermal diffusivity are obtained by comparing the experimental data with those from the numerical model. A discussion on error analysis is also made at the end of the Chapter.

Lastly, Chapter 6 summarizes the present concept and proposes future research directions and paths.

2. Experimental Set-Up

The experimental system presented in this work is custom-designed and built based on the laser flash technique. The main components include a high powered Nd:YLF laser pulse system, a linearly-polarized CW He-Ne probe beam, a small thin silicon wafer (diameter of about 4.0mm), two photo detectors, a voltage amplifier, a lens, a beam splitter, a data acquisition card, an oscilloscope and a black hardboard enclosure.

2.1 Overview of Experimental Set-Up and Main Instrument Components

The experimental set-up is shown in Figure 4. The sample is heated with a Nd:YLF laser system that outputs up to ~16mJ at 1 Hz with a wavelength of 527nm. The pulse duration is about 172 ns.

Meanwhile, an intensity-stabilized CW He-Ne laser such as a Micro-g LaCoste ML-1, with a wavelength of 632.8nm, serves as the probe beam. The laser has a 1mW linearly polarized output with an active feedback system to maintain the output intensity to ±0.005% over a minute and considerably less over 1 minute. The signal detection is obtained using two low-noise Melles Griot photodiodes and a low current Melles Griot voltage gain amplifier. The two photodiodes, a 'signal' diode measures the current of the reflected beam from the back of the sample and a 'reference' diode measuring the current from the incident probe laser beam via a BK-7 glass beam splitter. The two signals from the two diodes are eventually coupled together to balance out the two incident intensities

so that the balanced output current is zero. Reference and signal beam intensities are adjusted based on the incident angle and choice of beam splitter. Two manual shutters, or apertures are mounted directly on each diode to minimize any stray light. A filter can also be used as a method to balance the current in the two diodes.

Since the current signal is low, it is amplified using a gain amplifier and subsequently converted into a voltage signal. The amplified voltage is then sent to a high precision (16-bit) high speed (250Ms) digitizer and PC for data collection and analysis. Labview is used for data acquisition while the post-processing of the data will be done on ANSYS. The entire experiment is built on a vibration-isolated optical table covered with a 22”x 13” x 12” black hardboard enclosure to eliminate noise from stray room light and reduce air motion. The enclosure is also ideal to protect delicate optical instruments. A digital controlled water chiller could be used to provide temperature control within the enclosure but this is not strictly necessary because the rise in temperature occurs in a very short amount of time.

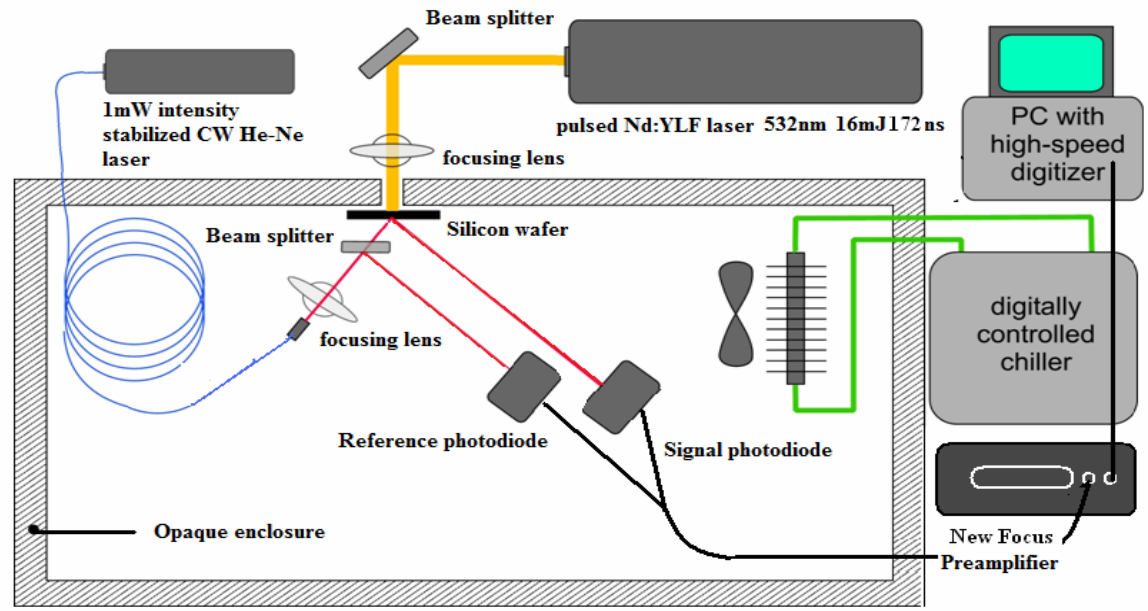

Figure 4: Main components of the experiment

An optional dry nitrogen purge can also be used to further improve measurement consistency.

2.2 Choice of Test Sample

The sample in the experiment can be chosen among different materials, however several properties are desirable. These include the bottom (or rear) surface to be optically smooth to specularly reflect the probe laser. The sample material should have a relatively large reflectivity with temperature, in other words, $\frac{d\rho}{dT}$ should be large. For the purpose of the work, the sample should be inexpensive and readily available.

Substrate	Type	$d\rho/dT$ (0^o incidence)	Ref	Wave-length	Comments
silicon	Free-standing	4.9×10^{-5}	[22]	633 nm	Inexpensive, easy to get, easily cut; but relatively small $d\rho/dT$, may oxidize over time. No transparent substrate required.
Cu	Thin film on glass	21×10^{-5}	[23]	690 nm	Easy to fabricate and inexpensive but but requires transparent substrate
Al	Thin film on glass	45×10^{-5}	[23]	690 nm	Requires transparent substrate
TiN	Thin film on glass	16×10^{-5}	[24]	770 nm	Very hard, high-temperature-deposition tolerant; but harder to obtain.

Table 2: Choice of test sample available

The sample material can be either a free-standing, e.g. in the current experiment, or a thin metal film deposited onto a glass substrate, in which the metal film serves as the temperature dependent reflective surface. Free-standing films are easier to measure and analyze; coated-glass substrates are more versatile in their material choice. Several substrates are listed in the Table 2 above.

Based on the advantages each substrate provides, Si-wafer is used in this work because wafers are readily available and are free-standing. Ultra-thin silicon wafers can be obtained in dimensions of 50 mm (about 2 in.) in diameter and a thickness of about 50

μm. The wafer is slightly p-doped whose optical properties have been characterized [22]. The small pieces of silicon wafer used in this work were provided by Professor Cubaud and were doubled polished. They are about 76 μm thin.

2.3 Preliminary Results and Instrument Proof-of-Concept

To illustrate the validity of the thermoreflectance technique and establish a worst-case signal to noise (SNR) scenario, an Omega 10W 120V AC resistive heater was attached to the front side of the heater instead of the Nd:YLF laser. Data was collected with an existing 16-bit card at a rate of 20KHz. The heater was driven by an audio power amplifier at 60V with a 10KHz sine wave for 750ms. Data was collected for 200 ms prior to applying heater power to assess the quiescent noise in the system. A thin-thermocouple was also attached to the back of the wafer just above the illumination spot of the probe laser and served as a measure of the temperature rise in the film. This can be compared to the photodiode signal to asses SNR and sensitivity issues. This concept with the heated was performed in summer of 2006.

The results are shown below in Figure 5. The photodiode voltage is plotted versus time. There are three distinct regions in the graph: 1) 0-200ms, no heating, the signal represents noise floor, 2) the heater is energized. Since convective losses are small, the temperature increases linearly with time as power is provided to the heater, 3) heater voltage is terminated, wafer cools down by natural means. For this initial concept, the maximum rise in temperature on the back of the Si wafer was about 5.8ºC; hence the peak of the curve corresponds to a temperature of 5.8ºC. This is due to coupling of the 10KHz 60 Vrms heater voltage to the very high gain photodiode amplifier because they were sitting on top of one another. In the actual experiment, the laser, rather than the

heater will be used. The results below will later be used to validate the reflectivity models in Chapter 4.

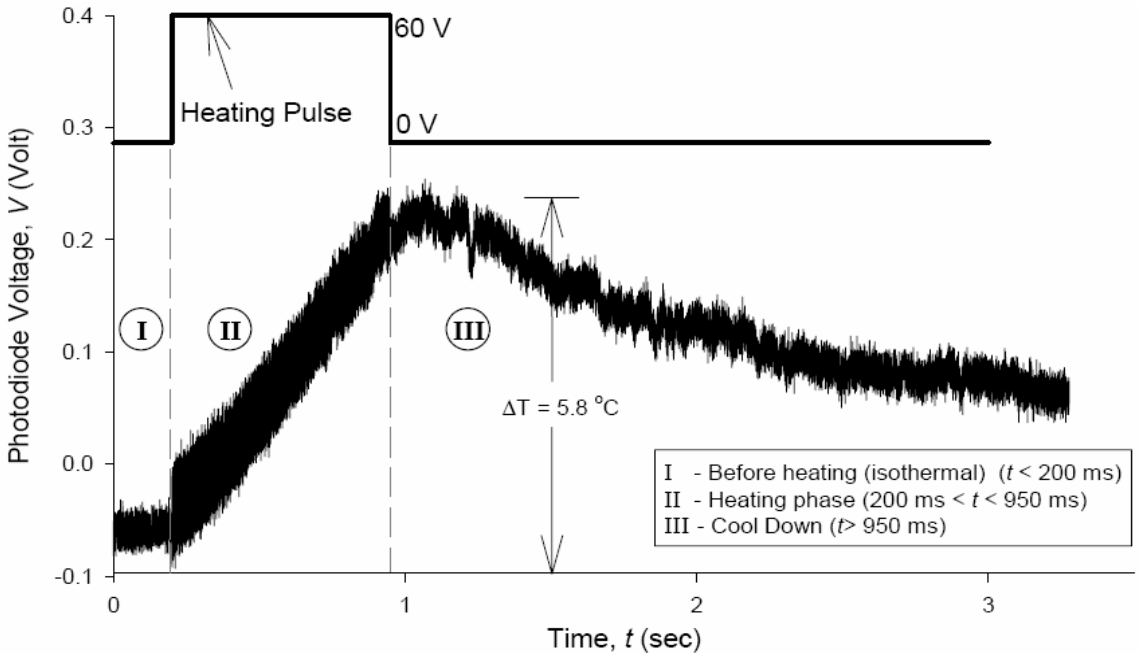

Figure 5: Photodiode output signal with a 10W resistive heater

3. Physical Model and Numerical Simulation

The reflectivity , ρ, of some solid material surfaces is a function of material refractive index, n, extinction coefficient, k (both in turn depend on temperature, T) and angle of incidence θ. The sample is taken to be in contact with a gas, e.g., air, with n = 1.0. A refractive index gradient will be formed if a temperature gradient is present in the sample under test. The probe laser beam incident on the wafer is deflected by the refractive index gradient, from which the thermal conductivity, k, and the thermal diffusivity, α, of the sample are determined by observing their influence on the measured time-dependent change in temperature on the rear surface. As such, the measurement is an inverse problem, in which the predicted thermal properties are compared with that recorded in the experiment.

Since the probe beam deflection is caused by the refractive index gradient as a result of the temperature gradient formed during a thermal pulse, the temperature distribution in the wafer is required to be solved first. Due to the complexity and difficulty of the analytical solutions, a finite element simulation of the heat conduction to quantify the temperature distribution in the wafer is performed. Afterwards, the mathematical reflectivity models of the probe laser beam are used to quantify the maximum rise in temperature in the present experiment.

3.1 Physical Significance of Thermal Conductivity and Thermal Diffusivity

Thermophysical properties can be classified into two categories: transport and equilibrium. Equilibrium properties such as temperature can describe a thermodynamic system with respect to a particular point in time. However, transport properties are those used to characterize systems under non-equilibrium situations. They always involve in the transfer of a specific physical quantity such heat, mass or momentum. From Newton's law, a driving force, or potential must be present to initiate such a transfer. Just as the concentration difference is the potential for mass diffusion, temperature gradient is the potential for heat transfer. The thermal conductivity is defined as in terms of Fourier Law, which was introduced by French mathematical physicist Joseph Fourier from his experimental observation in 1822 (Özişik, 1983). It is given in the form of

$$\vec{q} = -k\nabla T \tag{3-1}$$

where the thermal conductivity k appears as a proportionality factor between the heat flux vector $\vec{q}$ and the temperature gradient ∇T . According to Fourier law, the thermal conductivity is just the amount of heat conducted per unit time per unit area per unit temperature gradient. It has the dimensions of [Power] [Length]$^{-1}$ [Temperature]$^{-1}$.

Fourier law is valid for heat flow under steady-state conditions, while the heat diffusion equation that governs unsteady-state situations where the temperature varies with time t (Touloukian, 1973) is

$$\rho C_p \frac{\partial T}{\partial t} = k\nabla^2 T \,, \tag{3-2}$$

where k , ρ and C_p are the thermal conductivity, density and specific heat respectively. Equation (3-2) can also be rearranged to take the form of

$$\frac{\partial T}{\partial t} = \alpha \nabla^2 T \,, \tag{3-3}$$

where α is the thermal conductivity, and is defined as (Touloukian, 1973)

$$\alpha = \frac{k}{\rho C_p}, \tag{3-4}$$

with dimensions of. $[\text{Length}]^2[\text{time}]^{-1}$ The thermal diffusivity is an important property for heat diffusion in transient-state processes.

The combined parameter, ρC_p , in Eqs. (3-2) and (3-4) is also called the volumetric heat (Kim and Irvine, 1991). Equation (3-4) shows that a dependent relationship exists between these three parameters of thermal conductivity, thermal diffusivity, and volumetric specific heat. Given two of these parameters, the third can be determined from Eq. (3-4).

3.2 Thermal Model

As mentioned earlier, finding the thermal conductivity and thermal diffusivity is an inverse problem. A thermal simulation model of heat conduction with guess values of *k* and α needs to be established first to solve the temperature distribution within the wafer. Assuming the test wafer to have a cylindrical geometry and the thermal conductivity to be constant, the governing equations in cylindrical coordinates for 2-D heat conduction in the wafer is:

$$\frac{1}{\alpha}\frac{\partial T(z,r,t)}{\partial t} = \frac{1}{r}\frac{\partial}{\partial r}\left(r\frac{\partial T(z,r,t)}{\partial r}\right) + \frac{\partial^2 T(z,r,t)}{\partial z^2} + \frac{Q(z,r,t,)}{\alpha . C_p} \tag{3–5}$$

where $Q(z,r,t)$ is the input heat energy [mJ]. Based on Figure 6, the boundary conditions for Eq. (3-5) can be formulated as:

$$-k\frac{\partial T(0,r,t)}{\partial z} = q''(0,r,t) \quad , \; 0 \le r \le R \text{ and } 0 \le t \le \tau$$

$$= h\left[T(0,r,t) - T_\infty\right] \quad , \quad t > \tau \tag{3–6a}$$

$$-k\frac{\partial T(L,r,t)}{\partial z} = h\left[T(L,r,t) - T_\infty\right] \quad , \quad 0 \le r \le R_w \tag{3–6b}$$

$$-k\frac{\partial T(z,R_w,t)}{\partial r} = h\left[T(z,R_w,t) - T_\infty\right] \quad , \quad 0 \le z \le L \tag{3–6c}$$

where R , R_w and h stands for the radius of the heating laser, wafer and the convective coefficient of air respectively. The initial conditions for Eq. (3-5) are expressed below:

$$T(z,r,0) = T_\infty \tag{3–7a}$$

$$q''(0,r,t) = \begin{cases} \dfrac{E_p}{\tau.A} & 0 \le t \le \tau \\ 0 & t > \tau \end{cases} \tag{3-7b}$$

where T_∞ E_p and τ are ambient temperature in [˚C], the pulse energy in [mJ], and laser pulse width [nsl respectively. q'' is the heat flux generated by the laser pulse on the wafer. The heating surface area, A, which can be approximated to be circular is given by $\frac{\pi d^2}{4}$ where d =2R, the diameter of the heating laser pulse. Equation (3-7a) represents the wafer temperature before the heating pulse, equals to the ambient value, and Eq. (3-7b) defines the time-changing flux generated on the wafer during and after the heating pulse, respectively. Because the temperature profile of transient states are difficult to solve, the time-dependant solution is modeled using a finite element method package such as ANSYS and is discussed in the next few sections.

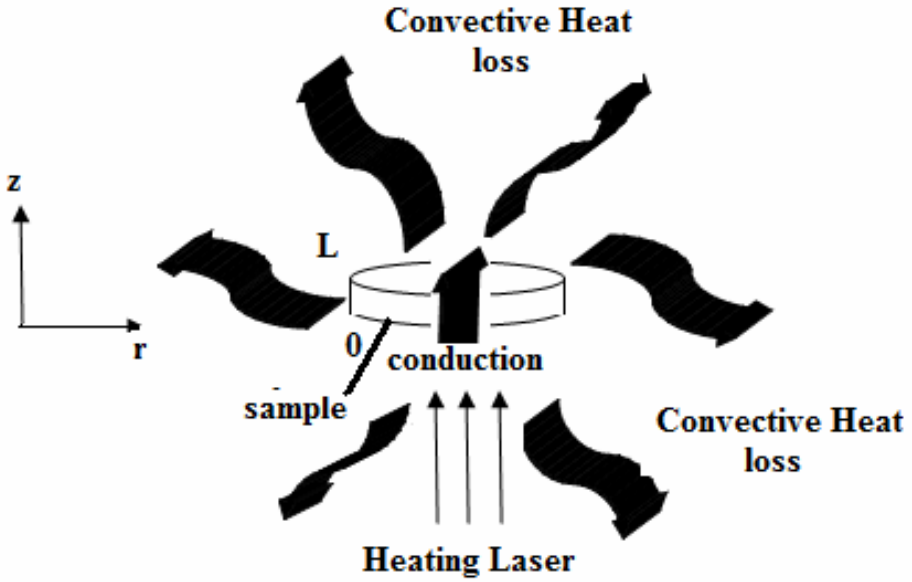

Figure 6: Thermal model

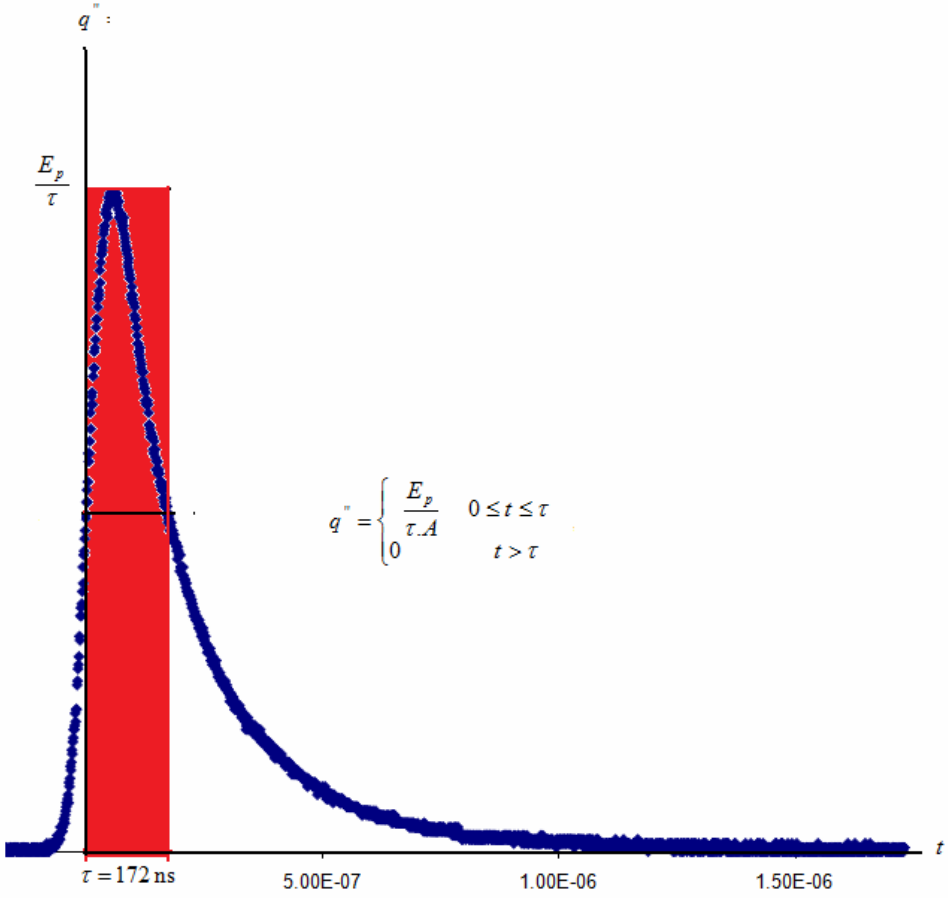

Figure 7: Heat flux generated by heating laser can be approximated in the form of a square wave

3.3 Optics and Ellipsometry

According to the electromagnetic theory, all light consists of transverse waves in which oscillating magnitudes are electric and magnetic vectors (Hetch, 1987). Referring to Figure 8 (top), assuming that a beam of light is traveling along the z-axis (end view) whose vibration is confined in the plane containing the z-axis and oriented at the some angle φ, although the sign and magnitude vary in time, is said to unpolarized. On the other hand, if the beam's electronic vector at some instant is executing a linear vibration with the direction and amplitude indicated (bottom) is said to plane polarized or linearly polarized. A plane of polarization of light is defined as the plane in which the electric

field or optical disturbance resides (Hetch, 1987). If the plane or polarization (vibration) is parallel to the plane of incidence, it is p-polarized light. Meanwhile, if the plane of polarization is perpendicular to the plane of incidence, it is s-polarized light. In nature light is unpolarized.

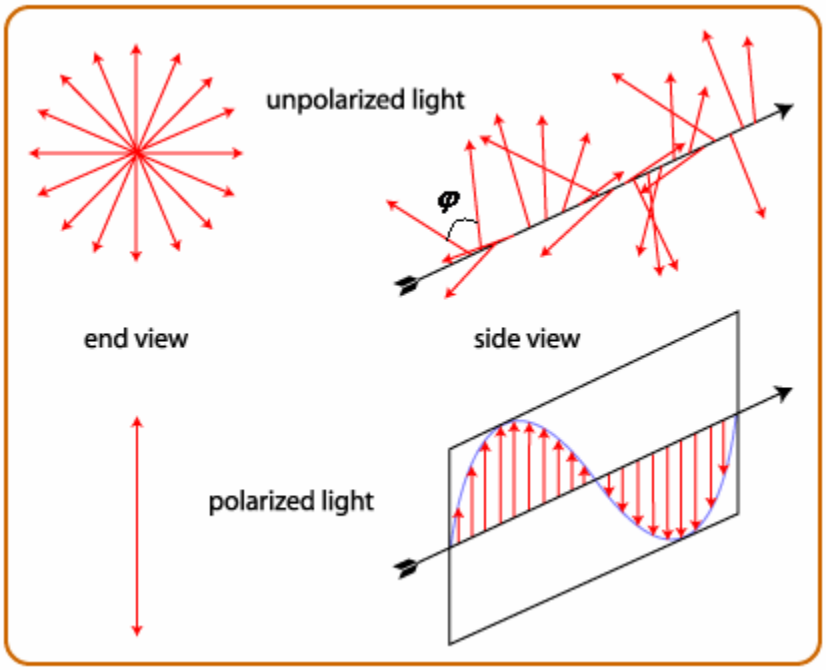

Figure 8: Vibration of unpolarized and polarized light

Light, like all electromagnetic radiation is a form of energy. The intensity if light is defined as the amount of energy that flows per second across the unit area perpendicular to the direction of light propagation. Whenever light strikes an interface, there is an energy transition involved. A certain amount of light energy is reflected into the first medium, while some energy is absorbed by the second medium. The rest is transmitted.

Reflectance, also known as reflectivity, is defined as the ratio of the reflected to the incident intensity (or power). It depends on the angle of incidence and light

polarization. According to Fresnel's law of reflection (Jenkins and White, 1976), the reflectance of s- and p-polarized light can be expressed as:

$$R_s = \left[\frac{\sin(\theta_i - \theta_t)}{\sin(\theta_i + \theta_t)}\right]^2 \tag{3-8a}$$

$$R_p = \left[\frac{\tan(\theta_i - \theta_t)}{\tan(\theta_i + \theta_t)}\right]^2 \tag{3-8b}$$

respectively. θ_i is the angle of incidence while θ_t, the angle of transmittance. Here the relationship between the angles of incidence and refraction follows Snell's law.

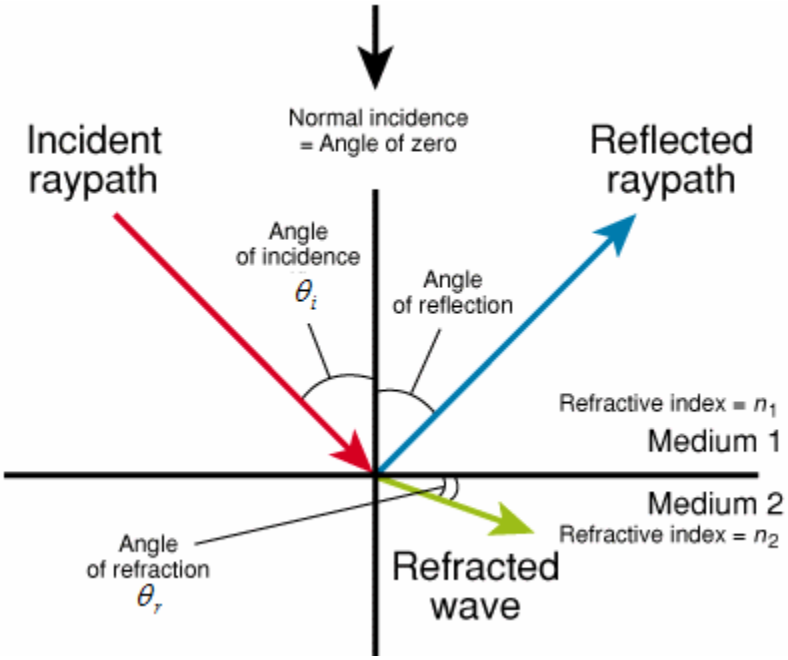

Figure 9: Reflection and refraction between two media

3.4 Thermoreflectance Model Measurement Principle

Referring to the Figure 10 (left), a deposited coating with refractive index, n_2 and extinction coefficient, k_2 are deposited into a non-absorbing dielectric substrate such as glass, quartz, or sapphire with refractive index, n_1 $(k_1 \approx 0)$.

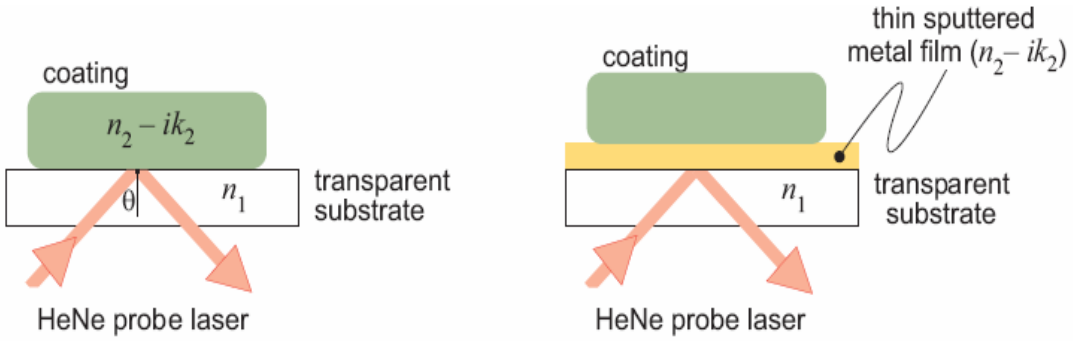

Figure 10: Thermoreflectance measurement principle

For a linearly polarized laser beam initially in medium 1 striking the interface at an angle θ, Fresnel equations (3-8a and b) predicts the reflectivity for parallel, ρ_p and the perpendicular, ρ_s polarizations [25] are:

$$\rho_s = \frac{(n_1 \cos\theta - p)^2 + q^2}{(n_1 \cos\theta + p)^2 + q^2} \tag{3-9a}$$

$$\rho_p = \frac{(p - n_1 \sin\theta \tan\theta)^2 + q^2}{(p + n_1 \sin\theta \tan\theta)^2 + q^2} \cdot \rho_s \tag{3-9b}$$

where

$$p^2 = \frac{\sqrt{(n_2^2 - k_2^2 - n_1^2 \sin^2\theta)^2 + 4n_2^2 k_2^2} + (n_2^2 - k_2^2 - n_1^2 \sin^2\theta)}{2}$$

$$q^2 = \frac{\sqrt{(n_2^2 - k_2^2 - n_1^2 \sin^2\theta)^2 + 4n_2^2 k_2^2} - (n_2^2 - k_2^2 - n_1^2 \sin^2\theta)}{2}$$

Both ρ_p and ρ_s are functions of n_1, n_2, k_2 and θ .They all are dependent on temperature. Thus if $\frac{dn_1}{dT}, \frac{dn_2}{dT}$ and $\frac{dk_2}{dT}$ are known, Equations (3-9a,b) can be used to relate time-varying changes in the reflected probe beam intensity to the coating-dielectric interface temperature history, which in turn is related to the coating thermal properties. Several materials have been identified as discussed in the next section.

The maximum temperature increase, ΔT at the coating-dielectric interface can be adjusted by varying the power of the heating laser. A typical ΔT will be 10-15ºC with a corresponding reflectivity change of $\frac{\Delta\rho}{\rho} \sim 10^{-4} - 10^{-3}$. A higher ΔT yields a larger $\frac{\Delta\rho}{\rho}$ but potentially introduce errors die to fact that the thermal properties are themselves temperature dependent.

As mentioned, an optional thin transducer layer made of AL, Cu, Ni., Pt, or other material can be evaporated or sputtered onto the dielectric substrate before the coating is deposited (Figure 10 right), which will provide a high-quality, specular interface and also provides the option to pick a metal that yields the largest $\frac{\Delta\rho}{\rho}$ based on its $\frac{dn_2}{dT}$ and $\frac{dk_2}{dT}$. Alternatively, the coating can be sprayed onto semiconductor–grade silicon, which will serve as both the substrate and optical transducer layer.

3.5 Numerical Solution of Heat Conduction

The time-dependant temperature profile, due to conduction, in the wafer is modeled using a finite element analysis package in the form of ANSYS. Initially, the analysis was performed using the PDE Tool command in Matlab. However, PDE tool is appropriate for only small and simple simulation of rectangular shape geometries. In contrast,

ANSYS provides a detailed simulation capability for complex geometries (cylindrical in this work). To model the heat conduction, the values of the material and thermal properties of silicon are obtained from literature, i.e., a density, ρ of 2330 kg/m^3, thermal

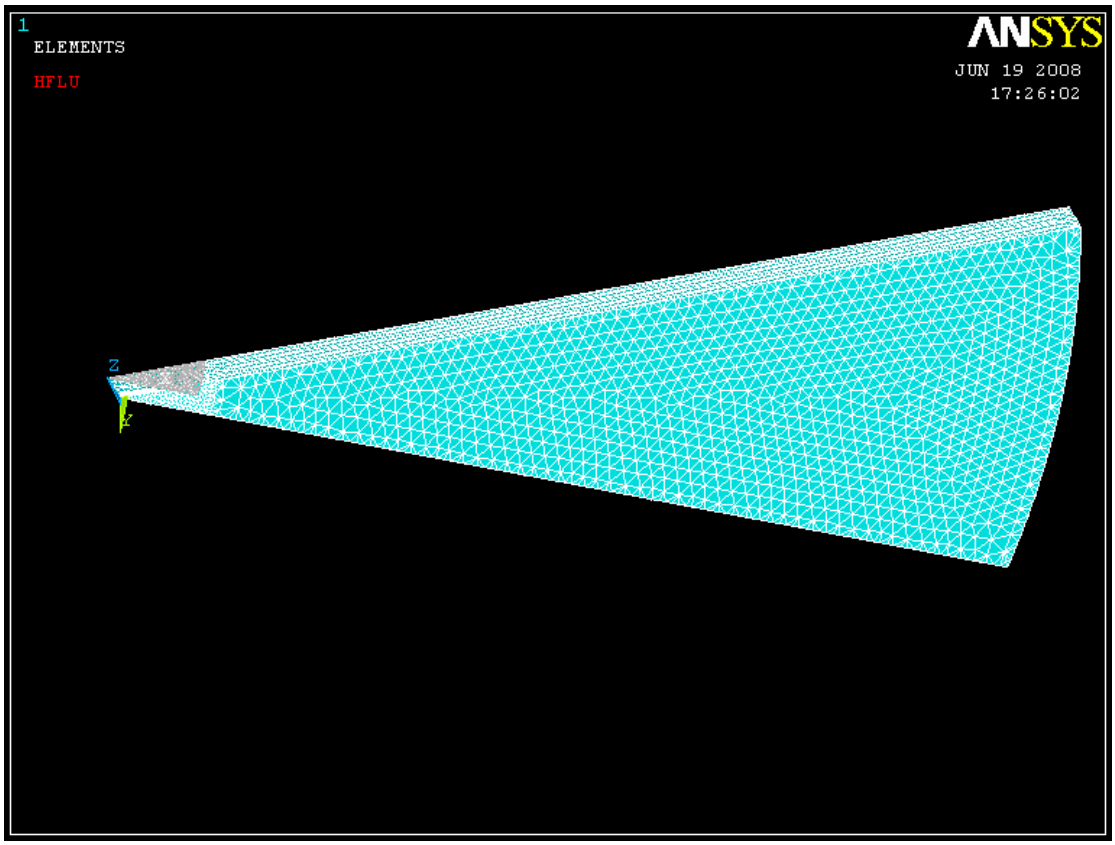

Figure 11: Finite numerical simulation performed on ANSYS

conductivity, k, of 140 W/m*K and specific heat, C_p of 700 J/kg*k. (In this work, the wafer may be doped and therefore the conductivity might be different). The thermal conductivity is modified later in the simulation so that the model's result comes to the best agreement to the experimental result. Since the test sample used was in the form of a circular disk, the model is designed and created based on cylindrical wafer geometry. The dimensions used correspond closely to that of the actual sample, a thickness of about

76μm and a diameter of about 4.0mm. The boundary condition and initial conditions are similar to those discussed in the above sections, i.e., the wafer is subjected to heat loss by convection around its surface, while the initial conditions are set to the following: 1) the initial temperature of the wafer is at ambient temperature, while 2) the heat flux from the laser is $\dot{q}$, at time $t \leq \tau$, and zero from time $t > \tau$, the laser pulse width. The varying heat flux is entered as a tabular 4 by 1 array representing four points around each corner of the square wave of the heating pulse as shown below:

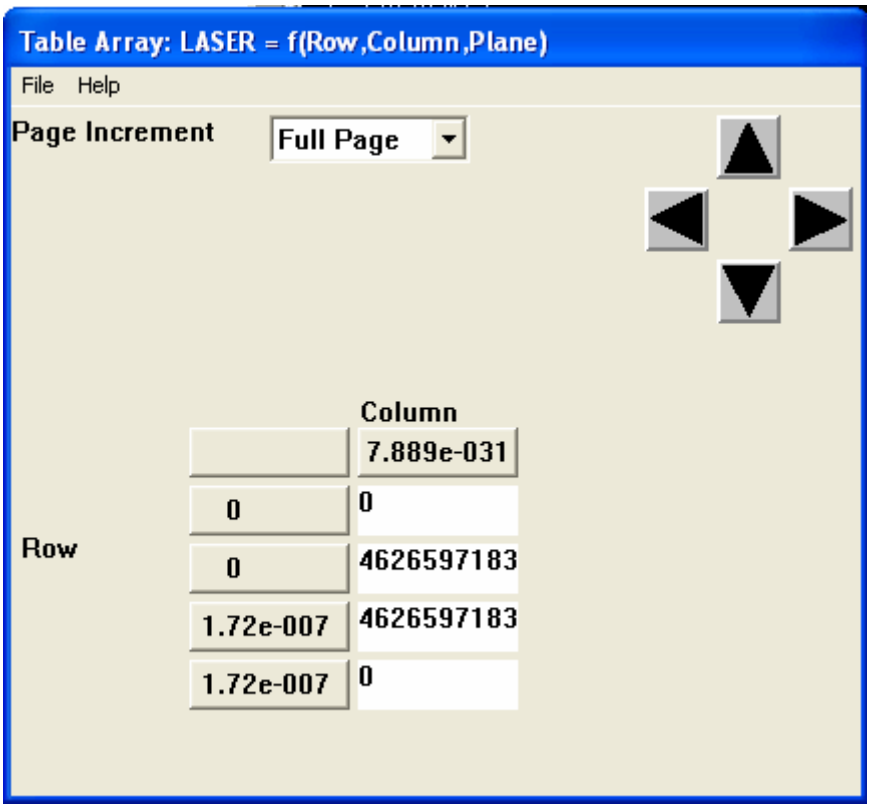

Figure 12: Varying heat flux in ANSYS

Because the heat conduction and convection process takes place in a very short time, the simulation is run for a total time of about 1-10ms. The meshing part is done in two ways; either using a uniform element length meshing throughout the model (inside the heating area, wafer and thickness of the wafer), or different element length for each.

In this work, a number of about 30-40 element nodes were chosen in the heating area and wafer region, while five element nodes made up the thickness. The element length is then determined using the dimensions of the model divided by the number of element nodes. ANSYS, however, complains if there are too many nodes especially at the curved surfaces. The average running time for the simulation is about 30-40 minutes. The more meshing there is (more refined), the more time it takes. Therefore, sometimes, the model is redesigned into reduced sections or fractions of the actual model (Fig.11), instead of the whole cylinder to save running time. To obtain as many data points as possible, especially in the rising (heating) part of the simulation, the total time is divided into three time increments; from 0 to $2*10^{-7}$s (within the laser pulse width), $2*10^{-7}$s to $6*10^{-4}$s and $6*10^{-4}$ to $1*10^{-2}$s. By choosing a number of steps of about 200-400 for the first two increments and about 50 for the last one, the step sizes can be calculated. Although ANSYS computes each number of steps that are input, they are not necessarily saved unless specified in the writing frequency command. Table 3 below summarizes the increments used:

Increments [seconds]	0 to $2*10^{-7}$	$2*10^{-7}$ to $6*10^{-4}$	$6*10^{-4}$ to $1*10^{-2}$
Number of steps	200	~399	~47
Step Size	$1*10^{-9}$	$1.5*10^{-6}$	$1*10^{-4}$
Writing Frequency	1	1	2

Table 3: Simulation time increments

Once the finite element simulation is completed, a nodal temperature in the middle of the wafer is picked on each side of the wafer (front and back) and imported in CSV-format

for post data processing. Alternatively, several nodal points along the heating area and wafer can be imported and plotted. A front and rear thermal profile, in the center of the wafer, is displayed in Figure 13. The maximum rise in temperature on the rear surface is about 282 ºC in about 42μs. To ensure the validity of the simulation package, the same simulation was done for a 1-D case. The maximum temperature rise and half-time are consistent with Parker's analytical model for 1-Dimensional heat conduction, except Parker's maximum temperature rise remained constant. In Figure 15, using linear interpolation, with known data points [127.2ºC, 9μs] and [172.6ºC, 12μs], the half time, $t_{1/2}$, corresponding to a temperature of about 141.1ºC, half the maximum, is determined to be around 9.91μs.

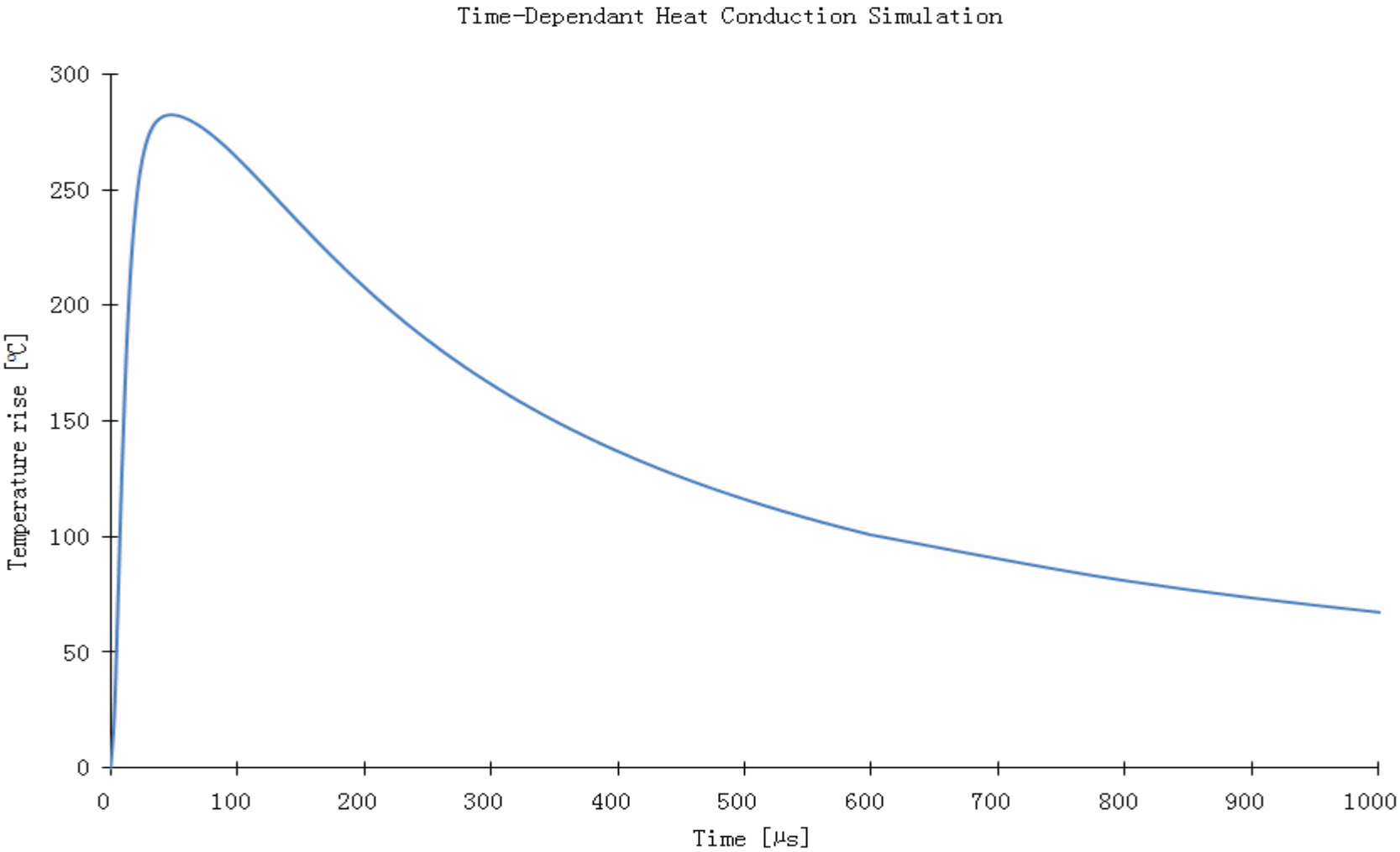

Figure 13: Backside temperature profile over a period of time of 1ms

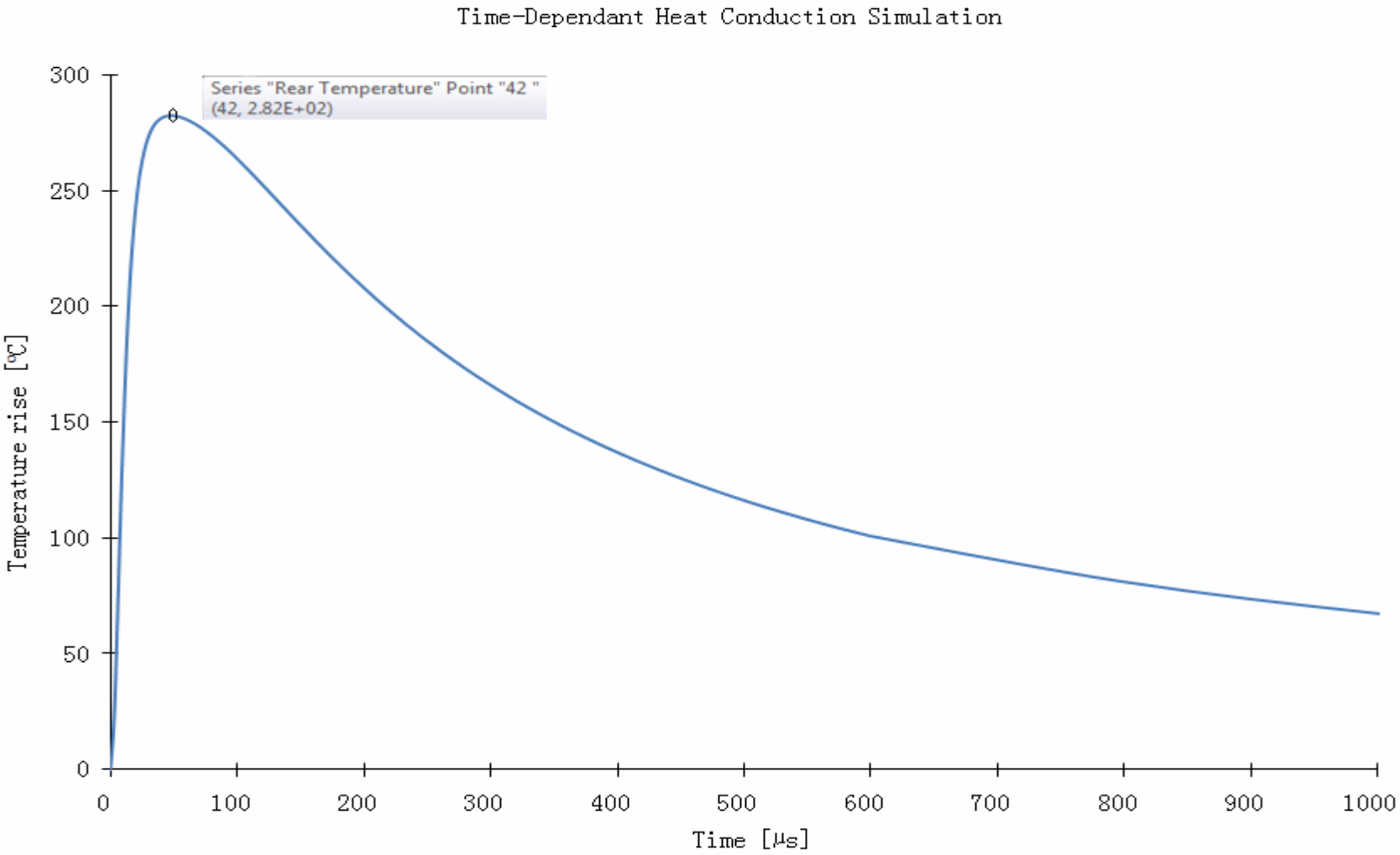

Figure 14: Maximum temperature rise of about 282°C in 42µs. Pulse Energy = 10mJ. Wafer Thickness = 76µm. Pulse Width = 172ns

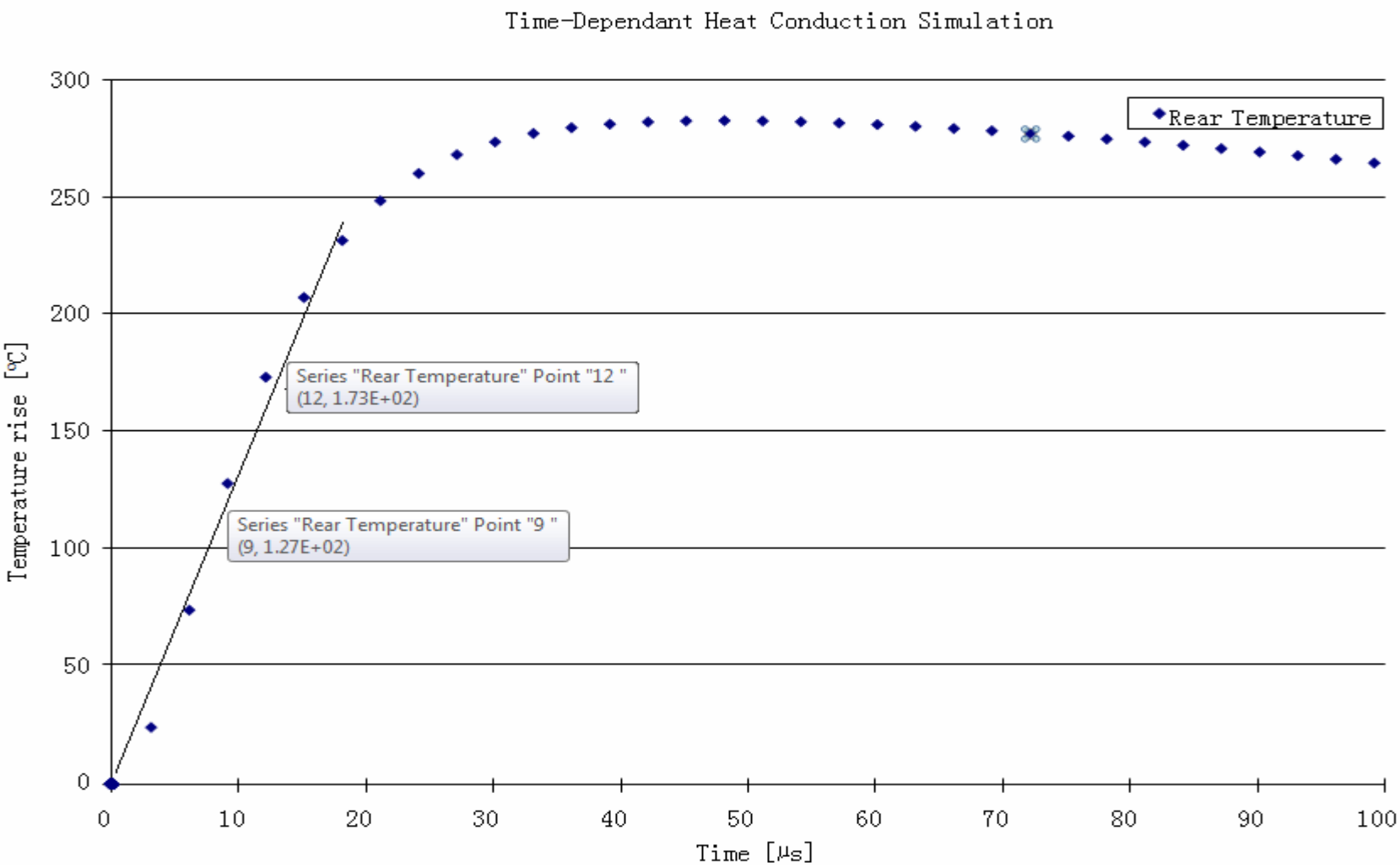

Figure 15: Heating part of the backside temperature profile with half-time, $t_{1/2}$ = 9.91µs

4. Experiment Models and Validation

A series of theoretical models and experimental verifications are performed to prepare for final data collection of the time-dependant temperature change. These include validating the reflectivity equations of the probe beam with the preliminary results and the actual reflectivity of the probe laser for p- and s- polarization. The two beam diameters, the heating pulse energy, pulse width as well as the silicon wafer thickness are measured. Finally, the two lasers, on either side of the wafer, are aligned as closely as possible using a special device called an electroviewer.

The reflectivity models are validated by comparing the gain in voltage from the probe laser beam models for p or s-polarized plane and the corresponding voltage signal value from the preliminary experimental result (Chapter 2). The voltage gain depends on the change in intensity of the reflected probe beam, which in turns depends on a change in reflectivity of the s- and p-polarized probe beam. Since the reflectivity itself is a function of the optical parameters that depend on a temperature change, the voltage gain can be related to a change in temperature.

4.1 Probe Beam Reflectivity Model Validation

The two media in this work are the interface of the silicon wafer and air, and their refraction indices are given as n_1 and n_2 where 1 and 2 represents air and silicon respectively. The value of n_1 is 1.0 while that of n_2 depends of the temperature of the silicon. Xu and Grigoropoulos [22] reported that:

$$n_2 = 3.84 + 4.90 * 10^{-4} T \tag{4-1}$$

where T is the actual temperature of the wafer at room temperature in ˚C. The extinction coefficient of air, k_1 is approximately zero while that of the silicon wafer, k_2 is temperature dependent as is given as

$$k_2 = 0.0221 \exp\left[\frac{T}{498}\right] \tag{4-2}$$

Thus at room temperature, the optical properties of silicon can be calculated as follows :

Medium	Refractive Index, n	Extinction Coefficient, k
[1] Air	1.00	0.00
[2] Silicon	3.85	0.023

Table 4: Refractive index and extinction coefficient of Silicon at 21˚C

Using equations (4-5) and (4-6) and the values of n_1, n_2, k_1 and k_2 above, the reflectivity, ρ, for s- and p- polarized probe laser beam are plotted against angle of incidence, θ and is shown in Figure 17. For an angle of incidence ranging from 0˚ to 90˚, the reflectivity for s-polarized plane gradually increases exponentially while that of the p-polarized plane decreases to a minimum and then increases more for a smaller change in angle of incidence. The angle corresponding to the 'dip' is known as the Brewster angle. For the wafer, the Brewster angle is found to be about 75˚ from the graph.

Theoretically, that could be verified using Snell's Law of reflection.

$$n_1 \sin\theta_1 = n_2 \sin\theta_2$$

For zero reflection (no light to pass), the incident angle, $\theta_1 = \theta_B$

Thus, $$n_1 \sin\theta_1 = n_2 \sin(90 - \theta_1) = n_2 \cos\theta_B$$

or $$\theta_B = \tan^{-1}\left(\frac{n_2}{n_1}\right)$$

$$\theta_B = \tan^{-1}\left(\frac{3.85}{1.00}\right)$$

$$\theta_B = 75.44°$$

The best angle of incidence, θ, would close to the Brewster angle where the reflection will be minimum. In Figure 17, the reflectivity changes very abruptly for angle to the right hand side of the Brewster angle (75˚ to 90˚), so by default an angle of incidence of about 70˚ is chosen for the experiment.

In order to find out the better plane of polarization, a comparison of the relative change in reflectivity for the two planes is determined. Equations (3-9a,b) can be rearranged into:

$$\rho_p(\theta, n_2, k_2, n_1) = \frac{(p(\theta, n_2, k_2, n_1) - (n_1 \sin\theta \tan\theta))^2 + q(\theta, n_2, k_2, n_1)^2}{(p(\theta, n_2, k_2, n_1) + n_1 \sin\theta \tan\theta)^2 + q(\theta, n_2, k_2, n_1)^2} \cdot \rho_s(\theta, n_2, k_2, n_1) \tag{4-5}$$

$$\rho_s(\theta, n_2, k_2, n_1) = \frac{(n_1 \cos\theta - p(\theta, n_2, k_2, n_1))^2 + q(\theta, n_2, k_2, n_1)^2}{(n_1 \cos\theta + p(\theta, n_2, k_2, n_1))^2 + q(\theta, n_2, k_2, n_1)^2} \tag{4-6}$$

where

$$p(\theta, n_2, k_2, n_1) = \left[\frac{\sqrt{n_2^2 - k_2^2 - n_1^2 \sin^2\theta)^2 + 4n_2^2 k_2^2} + (n_2^2 - k_2^2 - n_1^2 \sin^2\theta)}{2}\right]^{1/2}$$

$$q(\theta, n_2, k_2, n_1) = \left[\frac{\sqrt{(n_2^2 - k_2^2 - n_1^2 \sin^2\theta)^2 + 4n_2^2 k_2^2} - (n_2^2 - k_2^2 - n_1^2 \sin^2\theta)}{2}\right]^{1/2}$$

Since the reflectivity, ρ, is a function of n_1, n_2 and k_2 which depend on T, the total reflectivity as a function of incident angle is the given the sum of each partial derivatives of the three optical parameters and is shown as:

$$\frac{d\rho}{dT}(\theta) = \left(\frac{d\rho}{dn_1}(\theta).\frac{dn_1}{dT}\right) + \left(\frac{d\rho}{dn_2}(\theta).\frac{dn_2}{dT}\right) + \left(\frac{d\rho}{dk_2}(\theta).\frac{dk_2}{dT}\right) \tag{4-7}$$

For p-polarized light, using equation (4-5), the values of

$$\frac{d}{dn_1}\rho_p(\theta, n_2, k_2, n_1),\ \frac{d}{dn_2}\rho_p(\theta, n_2, k_2, n_1),\ \frac{d}{dk_2}\rho_p(\theta, n_2, k_2, n_1) \tag{4-8}$$

are calculated using a solving software such as MathCad. Moreover From equation (4-1 and 4-2):

$$\begin{aligned} \frac{dn_2}{dT} &= 4.9*10^{-4}.\frac{1}{C} & \Delta n_2 &= \frac{dn_2}{dT}\Delta T = 2.842*10^{-3} \\ \frac{dk_2}{dT} &= 4.629*10^{-5}.\frac{1}{C} & \Delta k_2 &= \frac{dk_2}{dT}.\Delta T = 2.690*10^{-4} \end{aligned} \tag{4-9}$$

where $\Delta T = 5.8^{\circ}\text{C}$. This was the change in temperature detected by the thermocouple and the reflectivity change in the preliminary result in Chapter 2. From Equation (4-7), n_1 does not depend on temperature, thus $\frac{dn_1}{dT} = 0$. Equation (4-7) simplifies to:

$$\frac{d\rho_p}{dT}(\theta) = \left(\frac{d\rho_p}{dn_2}(\theta).\frac{dn_2}{dT}\right) + \left(\frac{d\rho_p}{dk_2}(\theta).\frac{dk_2}{dT}\right) \tag{4-10}$$

Also, the change in reflectivity equals the change in partial derivatives,

$$\frac{\Delta\rho_p}{\Delta T}(\theta) = \frac{d\rho_p}{dT}(\theta)$$

This implies, $$\frac{\Delta\rho_p}{\Delta T}(\theta) = \frac{d\rho_p}{dT}(\theta) = \left(\frac{d\rho_p}{dn_2}(\theta).\frac{dn_2}{dT}\right) + \left(\frac{d\rho_p}{dk_2}(\theta).\frac{dk_2}{dT}\right)$$

$$\Delta\rho_p = \frac{d\rho_p}{dT}(\theta) = \left(\frac{d\rho_p}{dn_2}(\theta).\frac{dn_2}{dT} + \frac{d\rho_p}{dk_2}(\theta).\frac{dk_2}{dT} \right)\Delta T$$

$$= \left(\frac{d\rho_p}{dn_2}(\theta).\frac{dn_2}{dT}.\Delta T + \frac{d\rho_p}{dk_2}(\theta).\frac{dk_2}{dT}\Delta T \right) \qquad (4\text{-}11)$$

Combining, (4-9), (4-10) and ΔT , the change in reflectivity is:

$$\Delta\rho_p = 1.028 * 10^{-4} \qquad (4\text{-}12)$$

Similarly for s-polarized, $\Delta\rho_s = 2.010 * 10^{-4}$.

From (4-6), the reflectivity, $\rho_p(\theta = 70°, n_1, n_2, k_2)$ with refractive indices and extinction coefficient values obtained in Table 2, is found to be:

$$\rho_p(\theta = 70°, n_1, n_2, k_2) = 0.023 \qquad (4\text{-}13)$$

Experimentally, the reflectivity, P, can be measured by taking the ratio of reflected to incident powers of the probe beam using a Coherent FieldMaster GS™ Powermeter as shown in Figure 16. The experimental reflectivity turned out to be:

$$\mathrm{P} = \frac{I_R}{I_{I.}} = 0.075$$

The relative change in reflectivity, $\frac{\Delta\rho_p}{\rho_p(\theta, n_1, n_2, k_2)}$ can also be determined by diving results from (4-12) and (4-13). To find the voltage gain from the photodiodes as a result of a change in temperature, the intensity of the probe beam, the responsivity of the diodes and the gain factor associated with the New Focus amplifier is needed.

Figure 16: Powermeter to measure the experimental probe beam reflectivity

The voltage from the amplifier is given by:

$$V = I_R GR \tag{4-14}$$

where I_R the reflected power in [μW] is, G is the gain factor of the amplifier and is $\frac{4V}{200*10^{-9}A}$ and R is the photodiode responsivity with the value of $0.375\frac{A}{W}$ .The reflected intensity can be found from the following:

$$I_R = I_{I.}\rho_p \tag{4-15}$$

where $I_{I.}$ is the incident power. Combining (4-14) and (4-15), the voltage becomes:

$$V = I_I \rho_p GR$$

and thus the change in Voltage, $$\Delta V = \Delta\rho_p I_I GR \tag{4-16}$$

$$\Delta V = 0.283V$$

where I_I , G and R are constants. In Summary, for p-plane polarization, a change in temperature of about 5.8˚C will correspond to a corresponding change of about 0.283V in voltage signal.

Polarized Plane	S	P
$\frac{dn_2}{dT}\left[\frac{1}{°C}\right]$	$4.9*10^{-4}$	$4.9*10^{-4}$
Δn_2	$2.842*10^{-3}$	$2.842*10^{-3}$
$\frac{dk_2}{dT}\left[\frac{1}{°C}\right]$	$4.638*10^{-5}$	$4.638*10^{-5}$
Δk_2	$2.690*10^{-4}$	$2.690*10^{-4}$
Model: $\rho(70°, n_1, n_{2,} k_2)$ Experimental Reflectivity	0.693 0.641	0.023 0.075
$\Delta\rho$	$2.010*10^{-4}$	$1.028*10^{-4}$
$\frac{\Delta\rho}{\rho(\theta, n_1, n_{2,} k_2)}$	$2.903*10^{-4}$	$4.455*10^{-3}$
Incident Power, I_I [W] Reflected Power, I_R [W]	206μ 132μ	367μ 27.5μ
ΔI_R [W]	$4.141*10^{-8}$	$3.772*10^{-8}$
ΔV [V]	0.311	0.283

Table 5: Reflectivity model results for p- and s- polarized plane for DT= 5.8ºC

Repeating the same procedure, for the s-plane polarization, a change of 5.8˚C will give rise to a change of 0.311V. All values and results from the models are shown in Table 5 above. These values of ΔV obtained from the probe beam models appeared to be comparable to those obtained from the preliminary result. From Figure 5, the experimental voltage for same temperature rise was about 0.27V, while the models predicts a change of 0.283V, thus resulting in a deviation of about 4%. At this point, it can be concluded that the model is good enough for validation and the converting factor from voltage to temperature rise for p-polarized plane is 1V = 20.5 ºC

To validate the better plane of polarization, the plane with a larger relative reflectivity change is chosen, i.e., where $\frac{\Delta\rho}{\rho(\theta, n_1, n_{2,} k_2)}$ is larger. From results in Table 4, p-polarized plane shows a better change. Secondly, there is the Brewster angle, as explained above, is present in p-polarization only. Figures 18-20 below show the partial change in reflectivity with temperature, refractive index and extinction coefficient respectively as a function of angle of incidence. In all three cases, for an angle of incidence, say 70º, p-polarized plane results in better change (smaller values) than s-polarized. Figure 21 also displays clearly the angle of incidence selected, which is close to (left of) the Brewster angle (represented by the "jump"). The best angle would on either side of the "jump", keeping in mind it would very difficult to rotate the wafer to a very acute angle experimentally, i.e., on the right had side on the " jump".

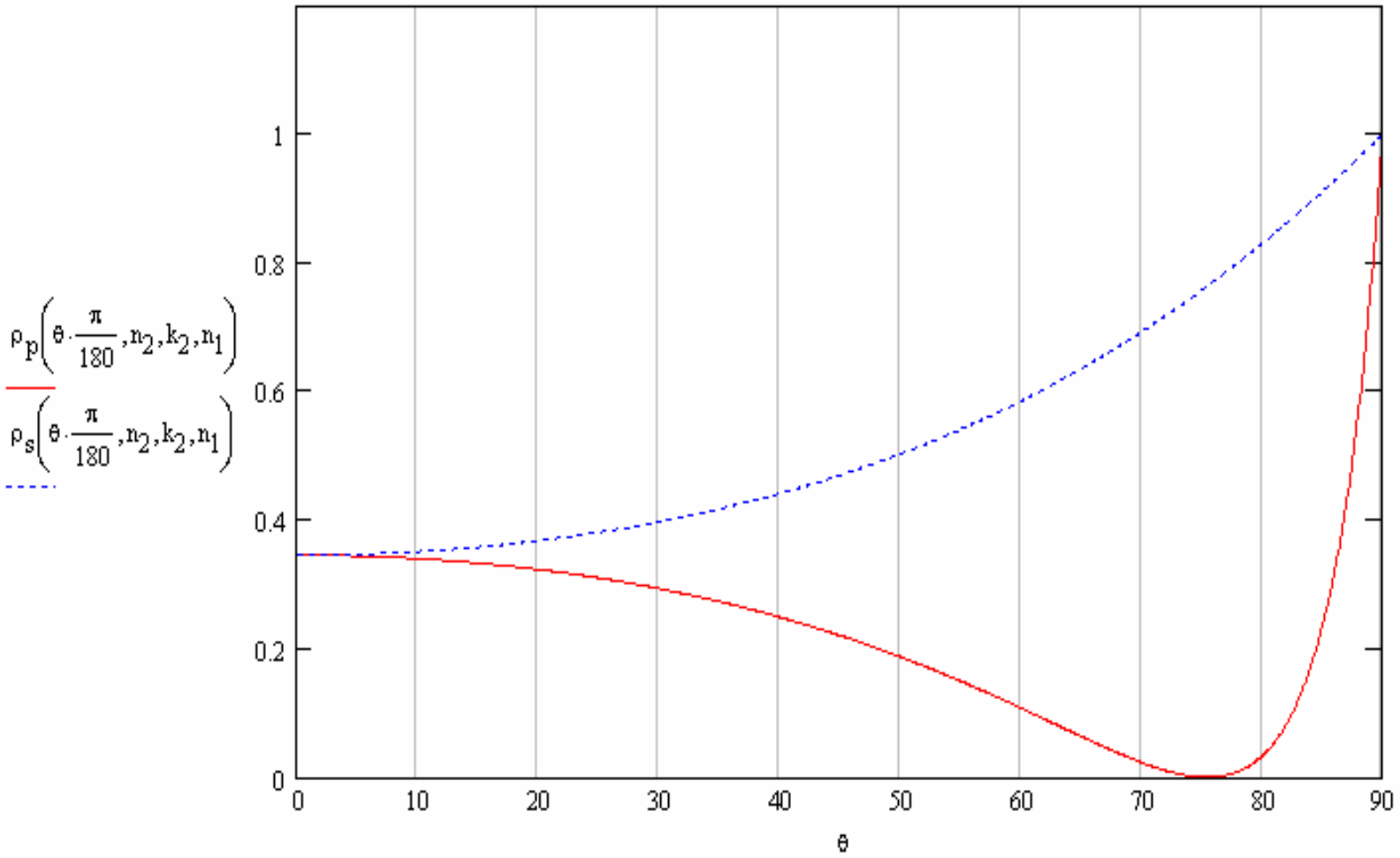

Figure 17: Reflectivity of the probe beam in s- and p- polarized plane as a measure of angle of incidence, θ

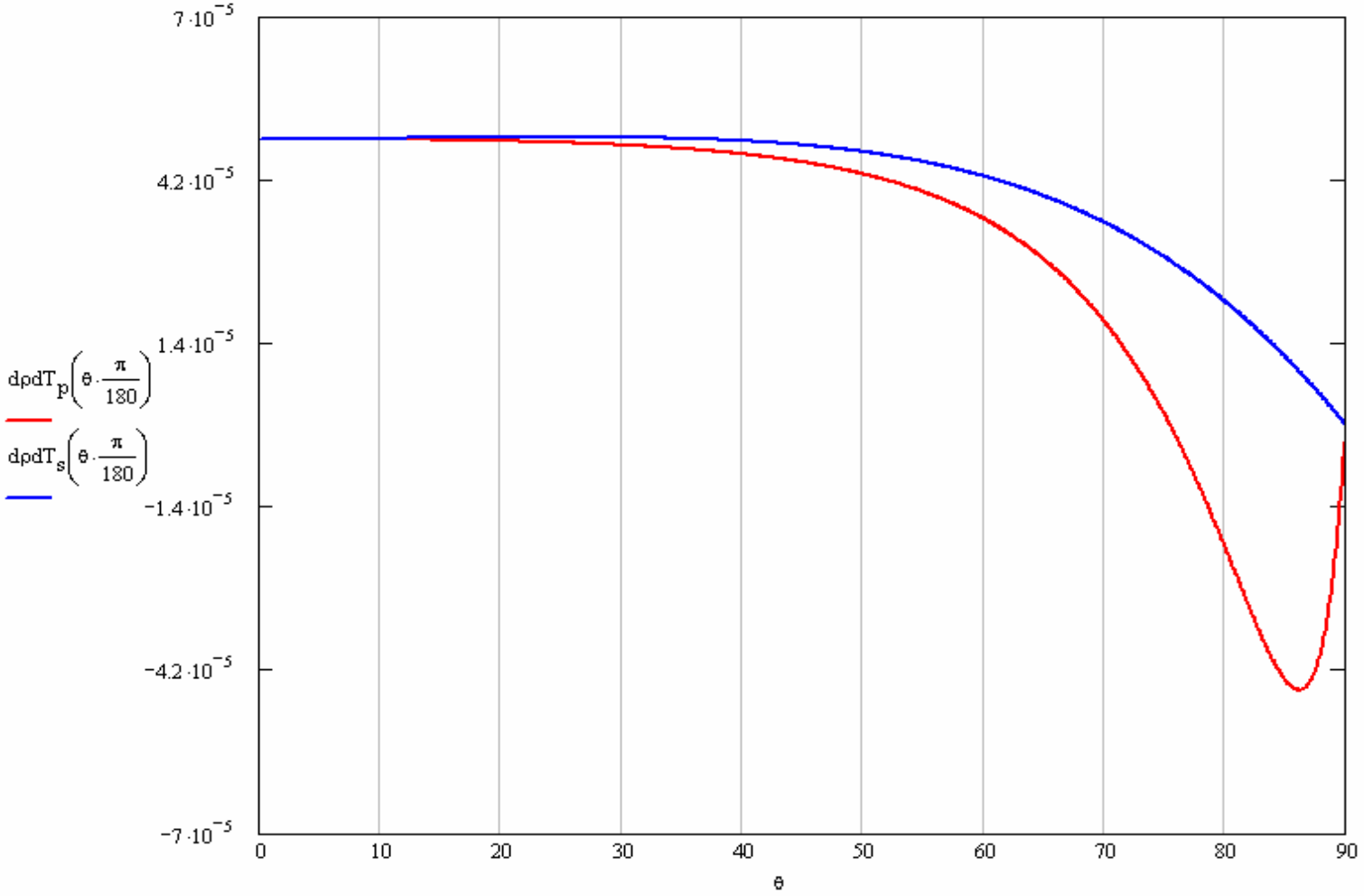

Figure 18: Reflectivity change w.r.t. temperature, $d\rho/dT$, for p- and s-polarization, with angle of incidence θ

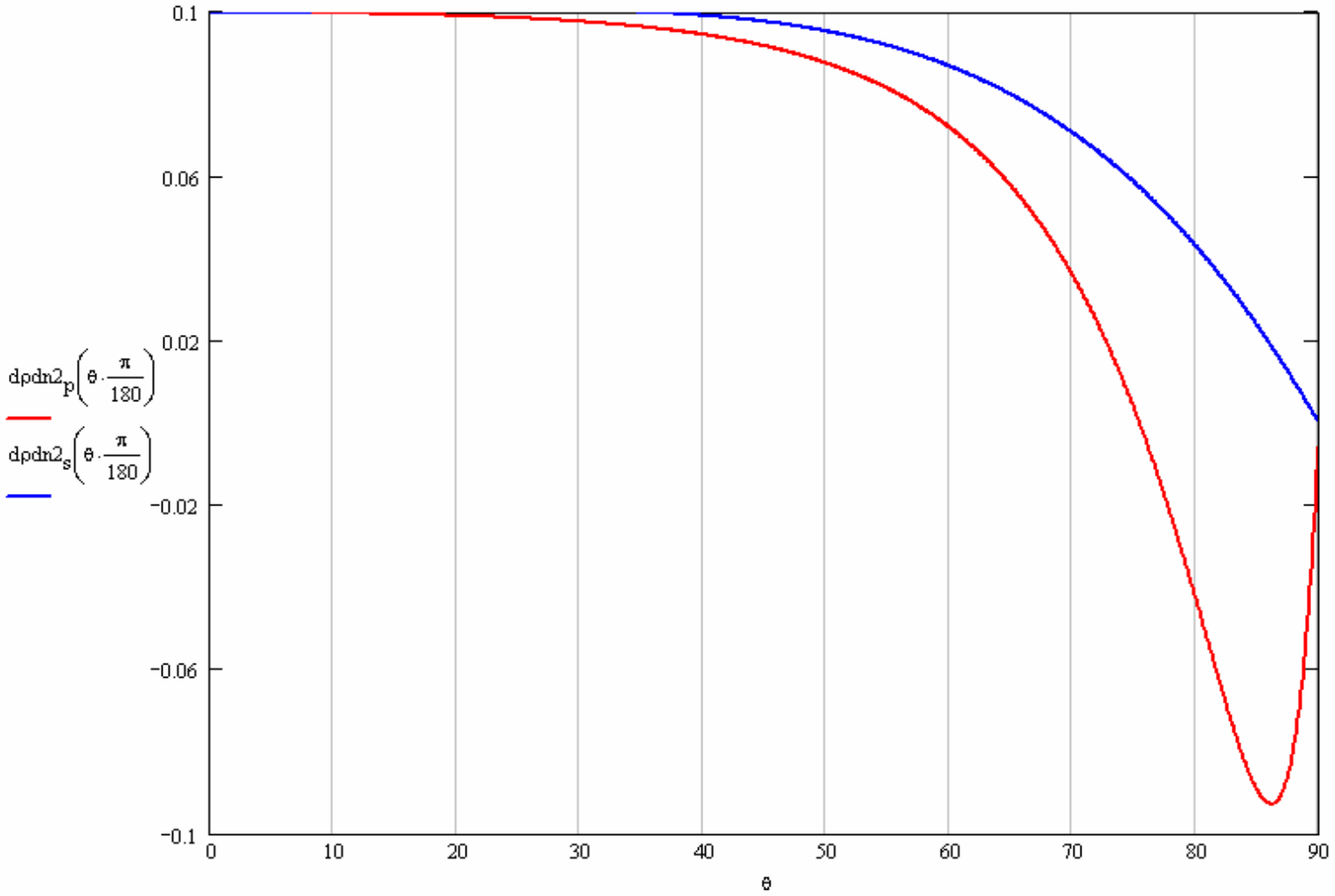

Figure 19: Reflectivity change w.r.t. index of refraction, $d\rho/dn$, for p- and s-polarization, with angle of incidence θ

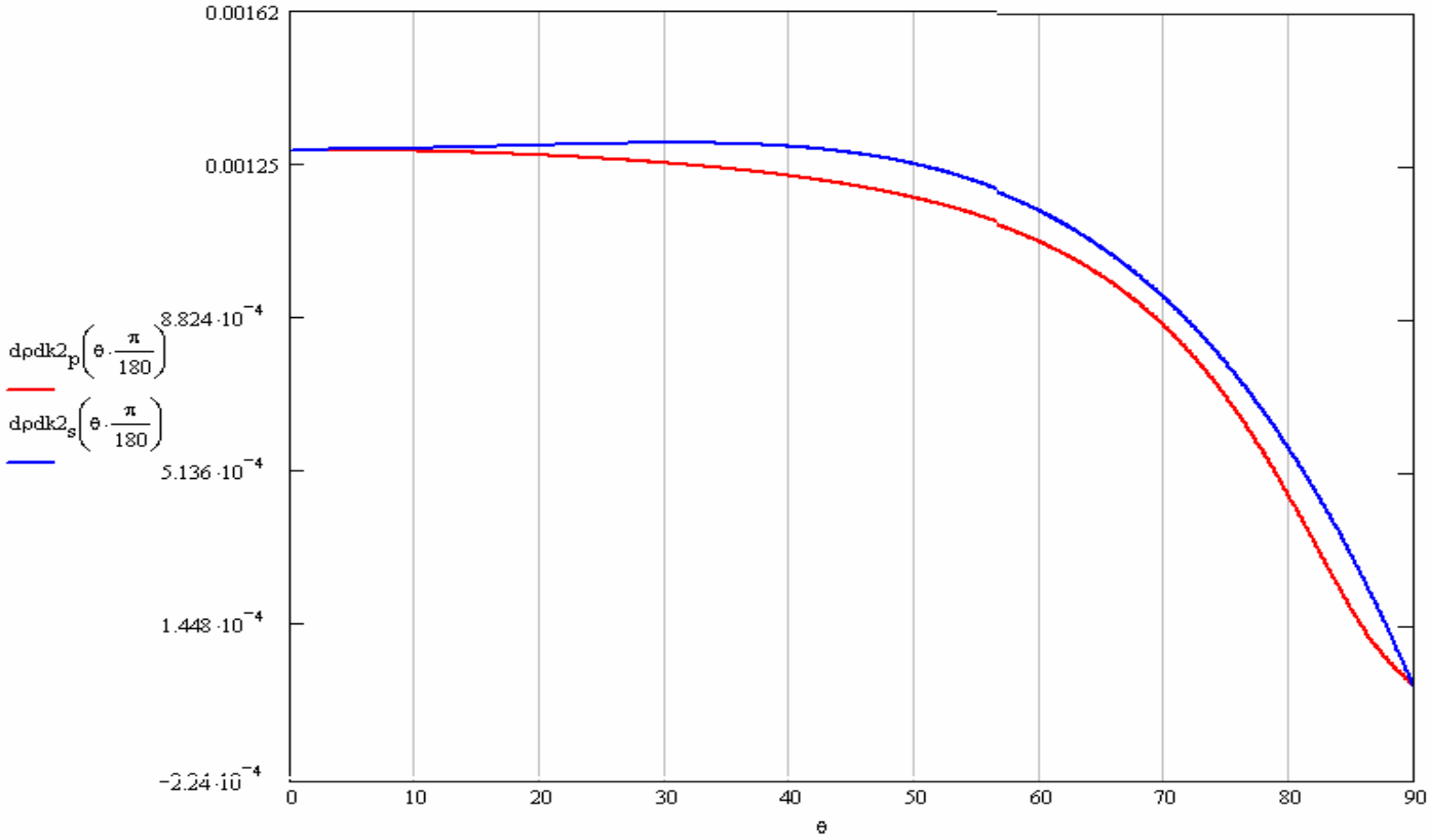

Figure 20: Reflectivity change w.r.t. extinction coefficient, $d\rho/dk$, for p- and s-polarization, with angle of incidence θ

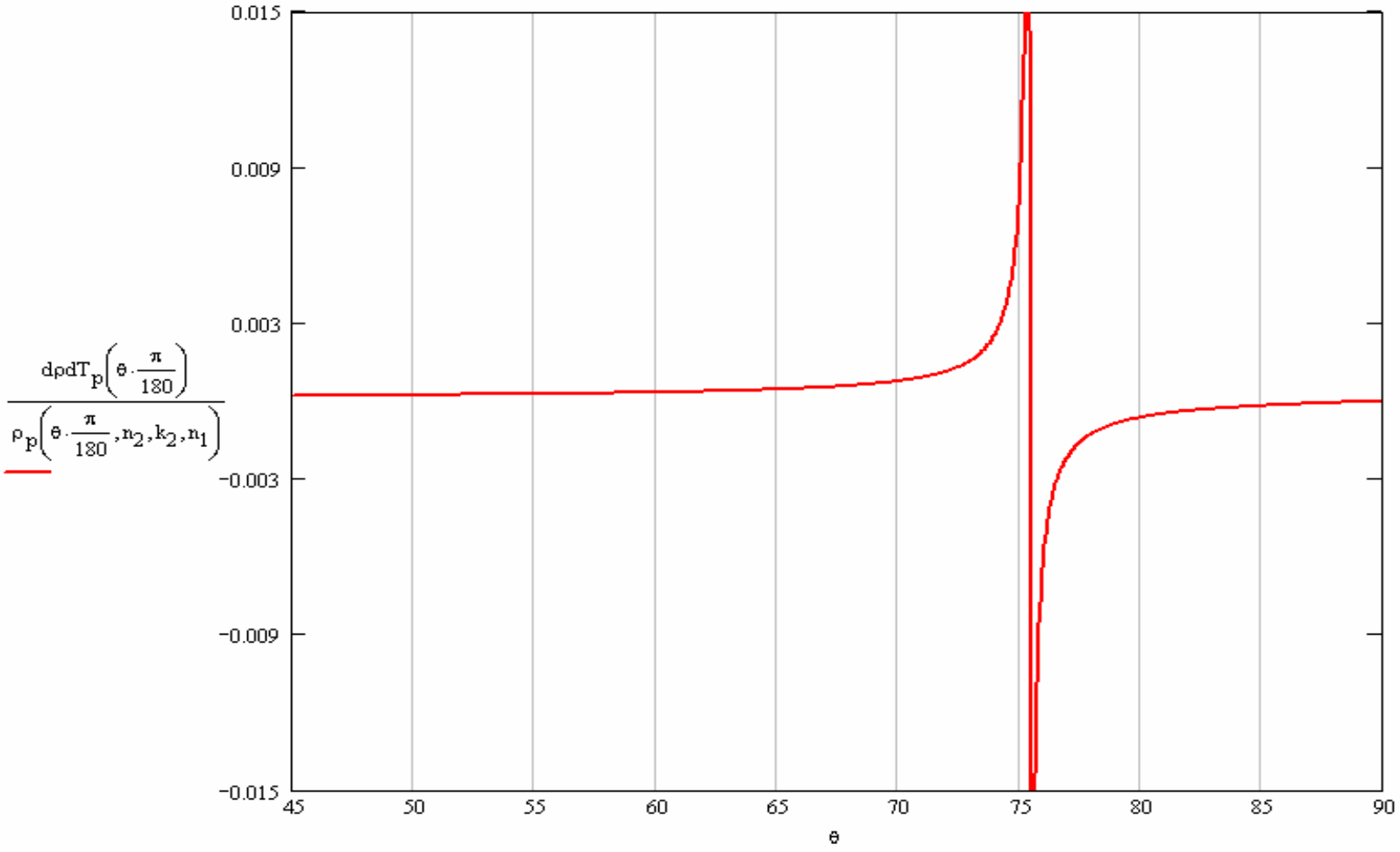

Figure 21: Relative change in reflectivity, $\frac{d\rho / dT}{\rho}$, for p-polarization, with angle of incidence θ

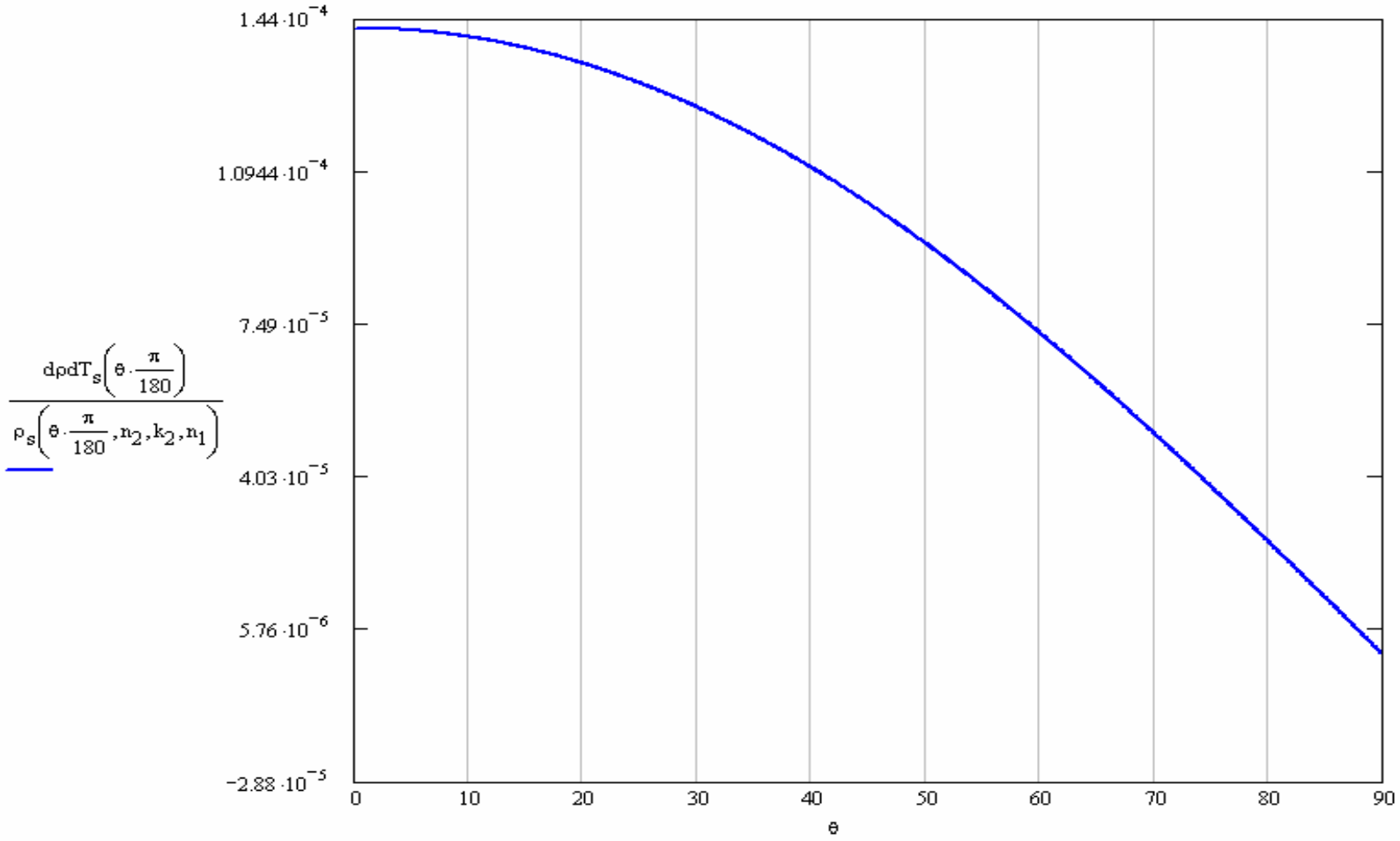

Figure 22: Relative change in reflectivity, $\frac{d\rho / dT}{\rho}$, for s-polarization, with angle of incidence θ

4.2 Verification of the two Laser Beam Diameters, Pulse Energy and Pulse Time Width

The probe laser beam diameter is measured using a special Digital Beam Analyzer, made up with a CCD Spiricon camera. The beam can be visualized in different profiles (and angles) as seen in Figure 23. As expected, the probe beam has the form of a Gaussian wave, with the maximum intensity at the centre, depicted by the red contour coloring, and decreases towards the edge. The measured diameter is 0.7139 mm. This measurement is also confirmed using a beam profile meter. Referring to the thermal model, the important parameters involved include the heating laser beam diameter, the maximum pulse energy and pulse time width.

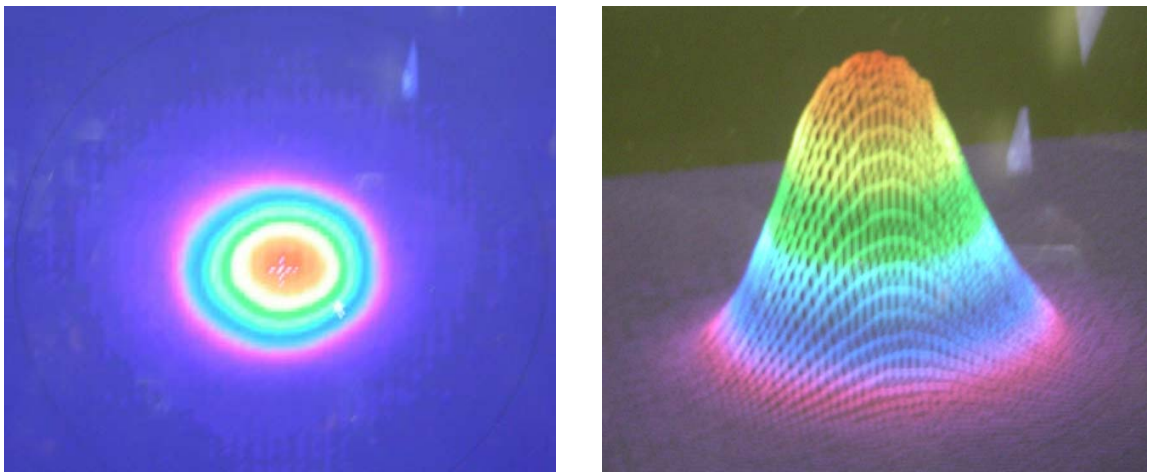

(a) (b)

Figure 23: Representation of the probe laser beam profile in (a) 2-D and (b) 3-D

This section presents one way to measure the heating laser beam diameter. This is achieved using a ZAP-IT alignment paper. The paper, shown below, is quickly swiped in the path of the laser beam so that a line of beam spots is traced on the black coating of the paper as shown in Figure 24. Using a microscope, the beams can be visualized and the diameter of each spot can be estimated. Figure 24 (Right) shows a schematic of the unique features observed inside each heating beam spot. It is very difficult to distinguish which part of the

beam spot is the actual diameter because each spot had a grayish color around a darker centre region. The diameter was estimated around the inner darker region and measured to be about 0.6 ± 0.1 mm. The heating laser has a special multi-mode pattern, unlike most other lasers which have a Gaussian profile. The pattern seems to represent a region of high and low "distribution" or intensity inside the laser beam. It is noted that the dark region is not located at the same location all the time (it could be way down the grey area, the middle or the top). Thus the intensity and therefore heating might be not uniform throughout its diameter.

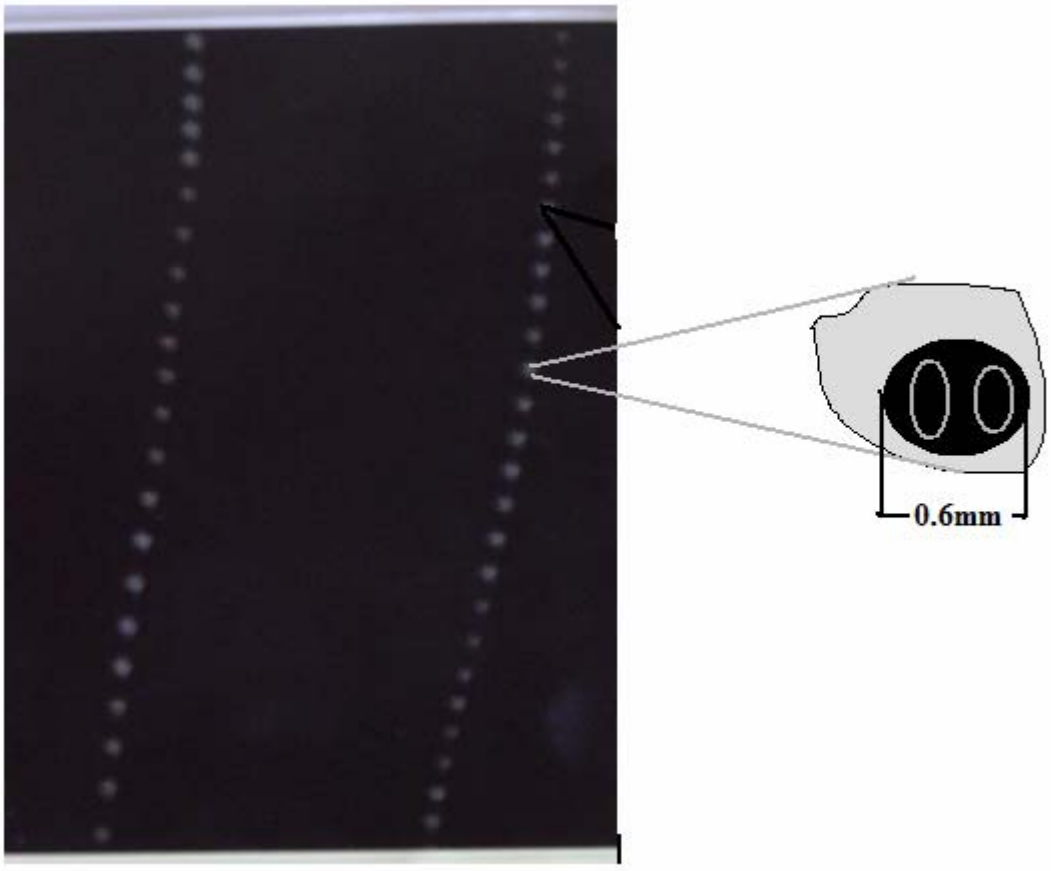

Figure 24: Alignment paper to measure heating beam diameter

The heating laser beam and also be visualized using the analyzer mentioned above. Figure 25 below shows the profile as seen by the camera.

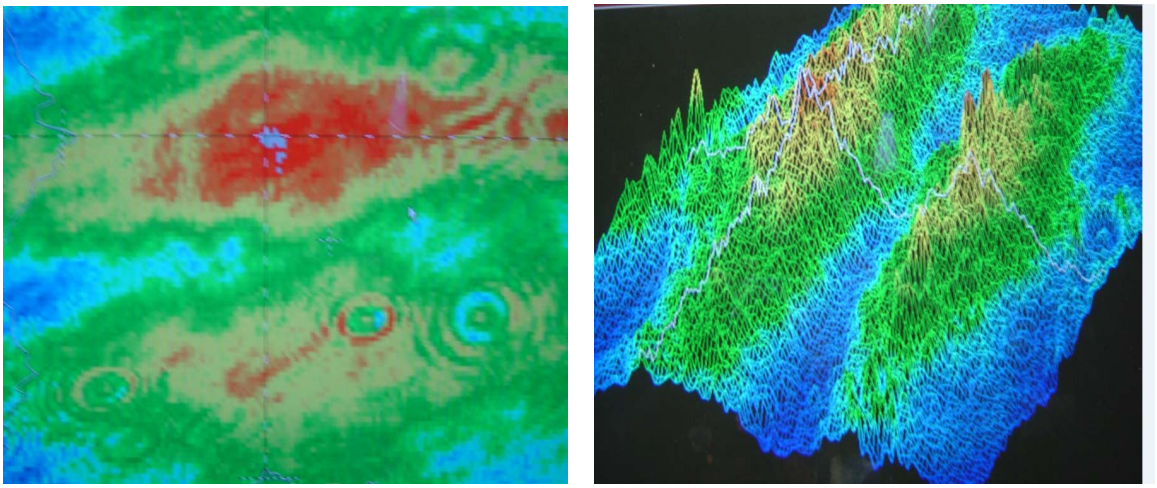

Figure 25: Heating laser beam profile

One important parameter of the Model GM 30-527 Nd:YLF-based laser system is its ouput pulse energy. The manufacturer's reported value of the pulse energy and power are 10mJ and 10W for a repetition rate of 1KHz. However it is noted that the pulse shape, output power and energy change with frequency. These values are verified using a function generator locked at different frequencies and the powermeter mentioned previously. The Nd:YLF laser being an old laser needs to have its power and pulse energy regularly checked after switched on. In other words, the laser system has to be calibrated and stabilized inside. Factors that could affect its power are: 1) the optics, the lens, front and back mirrors inside the Nd:YLF enclosure are cleaned regularly and properly aligned. Misalignment of the optics could result in slight deviation of the beam and affect the laser power. 2) The whole laser enclosure itself is properly positioned with respect to the table using a level. The enclosure rests on four bolt-like legs and the latter are securely clamped to prevent any movement from any loose support. 3) The laser lamp and hose cartridge connected to the controller box are changed regularly while any water pipe connection inside and outside of the laser enclosure are sealed-tight to

prevent any water leaks. After the laser is turned on, the system is warmed up for 30-45 minutes to obtain best results.

The whole experiment is run by the push of a single button inside the Labview software with a pulse rate of 1 Hz. To determine the output energy of each pulse, a simple calibration of the laser pulse for two different frequencies is made and their respective voltage signals are compared. Table 6 below summarizes the energy output of a single pulse. It can be seen for smaller frequencies (1Hz), the pulse energy is in fact greater than expected from the manufacturer's values. In other words, one would expect the pulse energy be 10 mJ for a single pulse (10W/1KHz) but realistically, the energy output of one pulse is much greater.

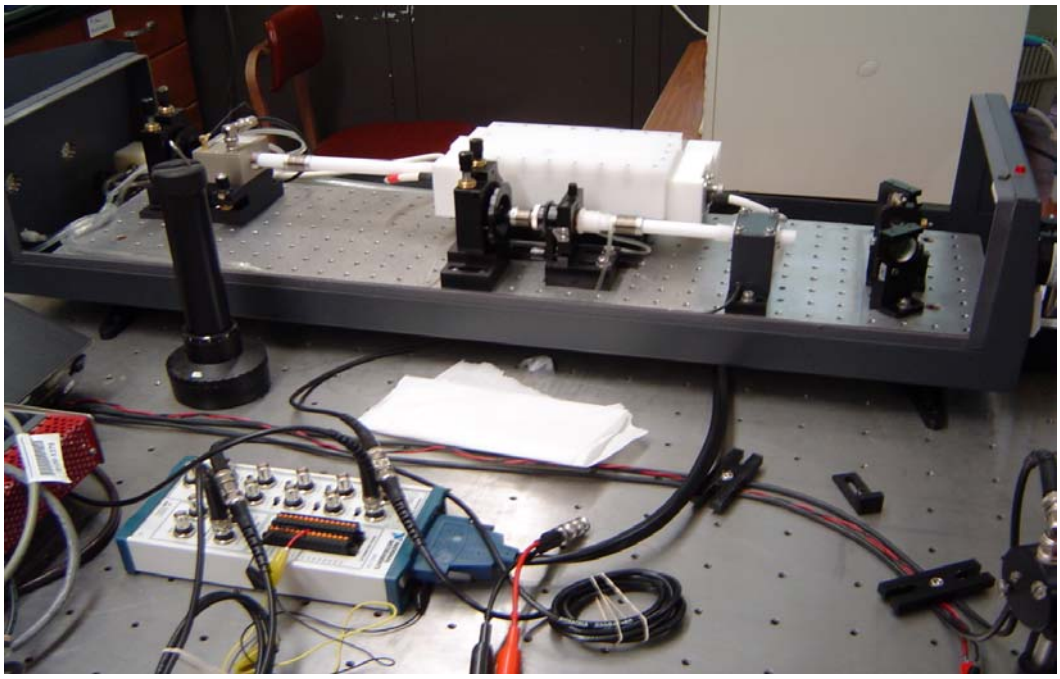

Figure 26: Inside view of the Nd:YLF heating laser system

With the help of a Tektronix TDS 380 (400MHz-2GS/s) oscilloscope, the peak voltage of a pulse at 1 Hz is measured to be ΔV_1 = 300-400mV (very fluctuating) whereas the voltage for

pulses at 1000Hz is $\Delta V_{1000} = 218\text{mV}$. Thus, $\Delta V_1 = 1.6\ \Delta V_{1000}$ meaning the energy output is in fact 1.6 times greater than 10mJ.

	Voltage measured [mV]	Power / Energy Output expected	Power / Energy Output measured
Multi-Shots[1KHz]	~218	10W	10W
Single-Shot[1Hz]	~300-400	10mJ	~16mJ

Table 6: Output Energy of a single heating pulse

However, since the Nd:YLF system is so intense that a lot of the energy is lost by reflection on the lenses and optical devices used in the experiment. The reflectivity of the heating laser is calculated to be about 32.3% (from the ratio of the reflected to the incident powers of the laser). Therefore, the pulse energy used for each trigger is about 67.7% of 16mJ, which is about 10.86mJ.

Similarly the pulse time width is also measured by connecting the laser controller box to the digital oscilloscope where the pulse profile is analyzed. Figure 27 below shows a typical pulse laser profile with a time width of about 172ns at half the maximum voltage.

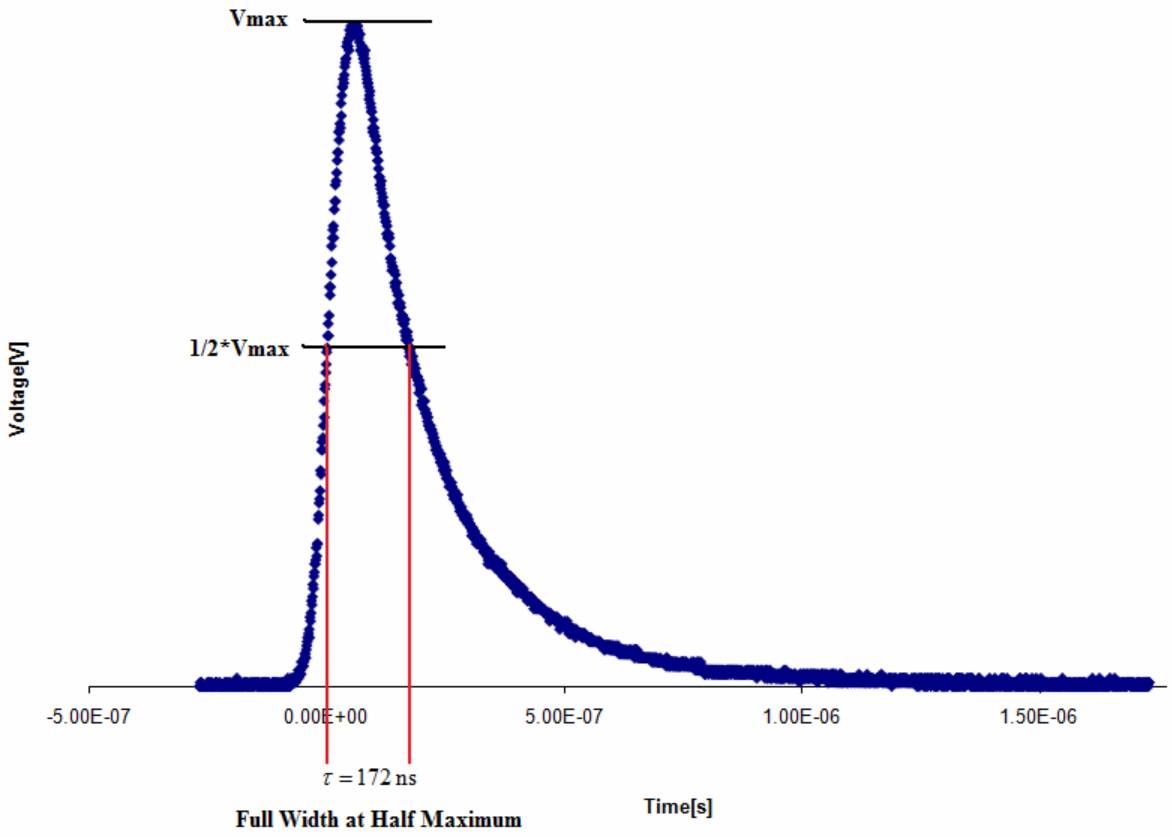

Figure 27: Oscilloscope reading showing pulse time width at half maximum

4.3 Verification of the Silicon Thickness

The most obvious choice to measure the thickness of the Silicon wafer is to use a caliper or a micrometer. However, with the help of Prof. Jon Longtin, a simple dial system was quickly set-up instead. The dial, shown in Figure 28, is calibrated to zero when the pin in the middle is level on the table. When the wafer is gently placed under the pin, the latter at the bottom moves up by a few microns corresponding to the thickness of the wafer. The wafer used is about 76µm ± 0.5 µm thick.

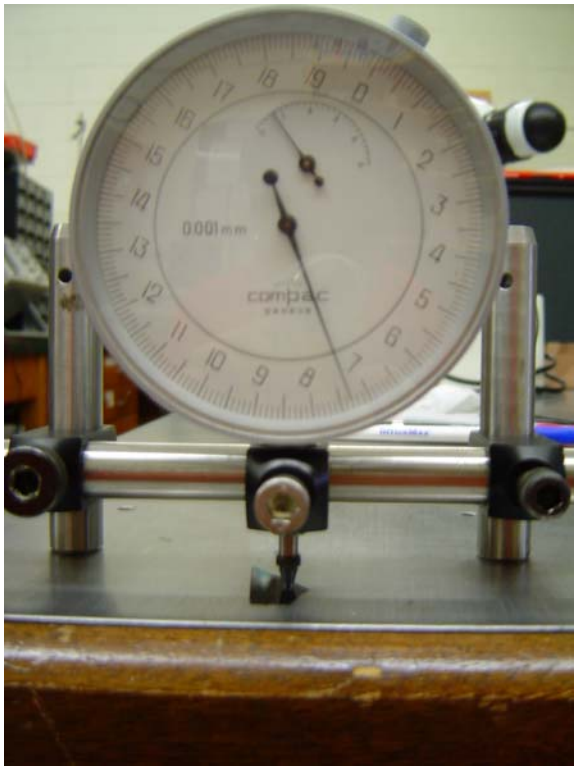

Figure 28: Pin dial indicator to measure the wafer thickness

4.4 Heating Laser and Probe Beam Alignment

One of the main obstacles encountered in setting up the experiment is aligning the two laser beams on, or close, to the same spot. This is achieved using an Electrophysics Model 7215 Electroviewer as in Figure 30. Because Silicon is an opaque material, no light can travel through it. At high power, the heating pulse emits enough energy, or infrared radiation, which can be viewed from the same side as the probe beam laser with the electroviewer. Like for any lasers, it is always advisable not to look directly into the path of the beam. Then the heating beam can be readjusted in three directions to match the probe beam spot. The former, focused on a 100mm-focal length lens, is mounted on a specially built three-axes translational stage as shown in Figure 29.

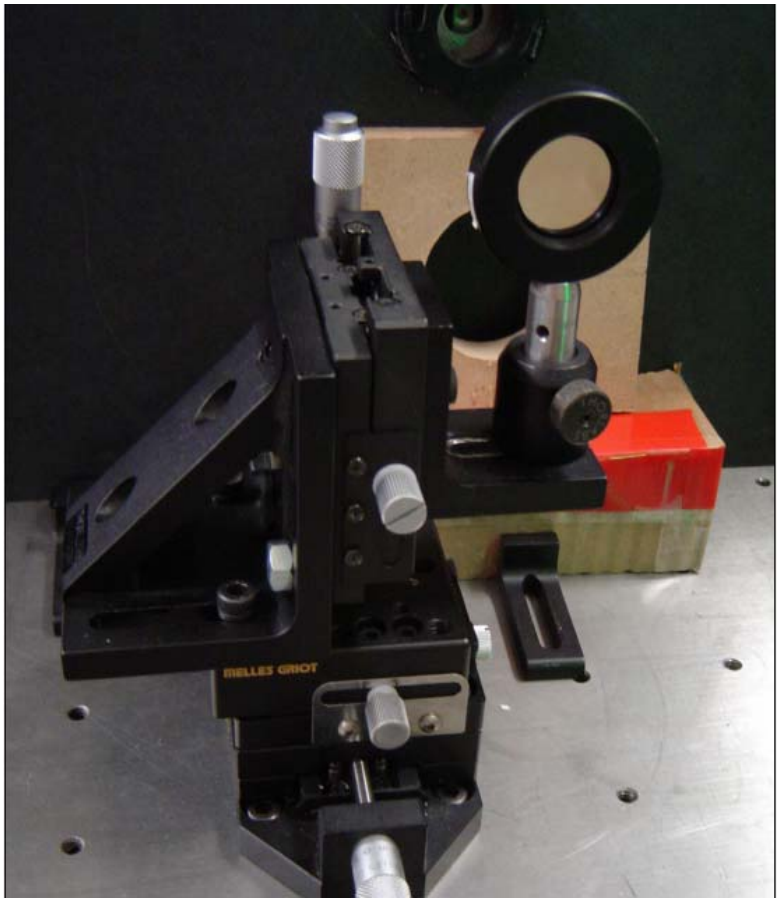

Figure 29: Specially-built translation stage with 100mm-focal lens

Thus the thermal signal can be observed when the two beams are close on the same spot. Unfortunately, aligning the beams with the electroviewer and moving the heating beam require assistance of two people.

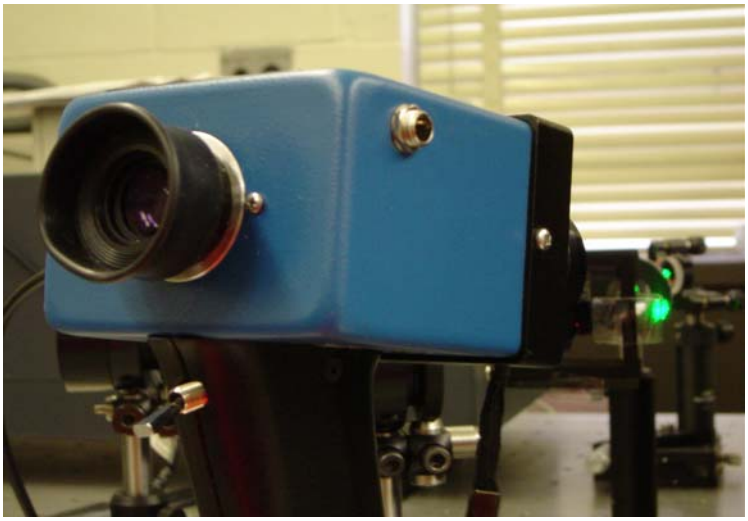

(a)

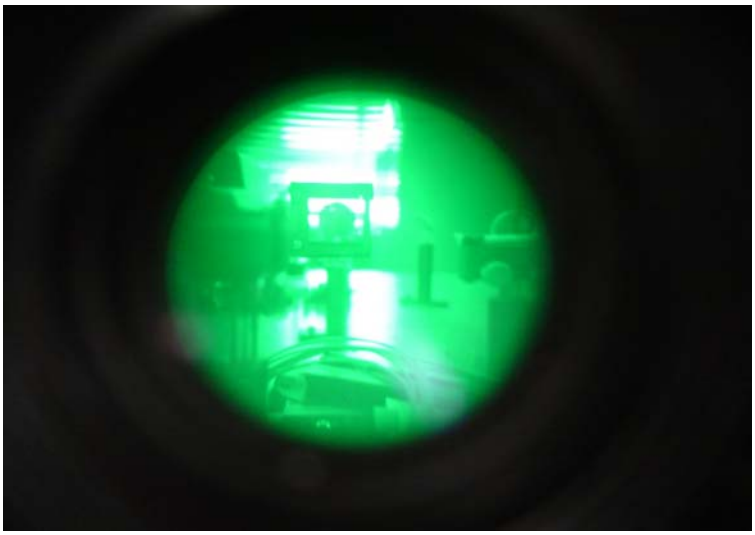

(b)

Figure 30: (a) Electroviewer to align heating laser pulse and probe beam (b) Inside view of the Electroviewer

5. Results and Discussion

After configuring and characterizing the system as discussed in Chapter 4, the experiment is conducted. Comparison between the experimental data and the numerical model results are then processed. The thermophysical properties of the wafer would then be adjusted to produce the best fit between the experiment and the model.

5.1 Data Collection and Processing

The time-dependant change in temperature of the backside of the wafer is recorded as an amplified voltage signal. Initially, the change in reflectivity of the probe beam produces a small photocurrent that is detected by the diodes. The current is then amplified and sent to Channel AI 1 of the 16-bit data acquisition card for data collection. The card can collect about $50*10^3$ samples at a rate of about 100 KHz. The card includes an internal voltage that \ outputs a 5V signal to its trigger input channel (Trigger Start Channel). That channel is then plugged into Channel AI 0 on the card, and is also connected to the heating laser controller box to trigger the laser. The Labview program, in Figure 31, uses a delay time of 100ms before collecting data. Once the acquisition completed, the program saves the data from both channels in XLS format for processing.

Another way to collect data is using an oscilloscope and a function generator. The same output voltage, from the amplifier, is connected to Channel 1 of the scope while the function generator outputs a square wave voltage to trigger the laser to Channel 2. The scope

can also be used for quick visualization of the signal and to make any necessary adjustments. A single heating pulse is used for each scope trace. The advantage of the scope is being able to run, save and repeat different experiments and performed different mathematical command such as averaging, amplitude measurements in both voltage and time durations axes. After the scope has completed the data acquisition, the data from both channels is saved in CSV-format for post-processing.

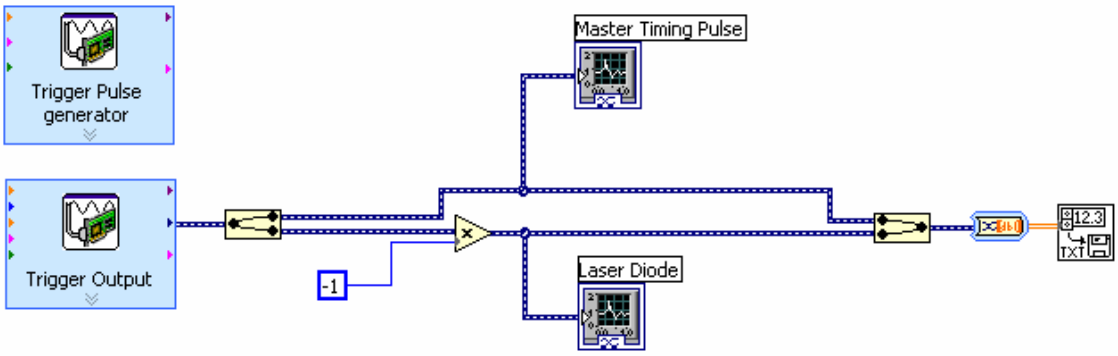

Figure 31: Labview program to collect thermal signal

Since k and α of the sample appear in Eqs. (3–5) and (3–6) as unknown parameters, substituting k and α with different values will result in different temperature gradients, and thus different time-varying probe beam reflectivity from the model. Therefore, k and α of the sample can be determined by searching for those values that yield the best agreement between the probe beam deflection from the numerical model and that recorded during the experiment.

5.2 Initial Results and Discussions

The first results obtained in the experiments were far from the expectations. The heat conduction profile: rise part due to the heating pulse and cooling section from convection, was absent. Instead an 'oscillating' signal with a high voltage was seen as shown in Figure 33. At first, one possible cause was due to vibration of the wafer when the heating laser pulse strikes the wafer. The silicon wafer, so thin, could oscillate due to a small force initiated from the laser flux. With the help of Prof. Longtin, a simple vibration simulation was modeled on Solidworks to verify if the natural frequency of the wafer, based on the wafer (material) properties such as modulus of elasticity and dimensions of the wafer is comparable to the values obtained from the oscilloscope.

Table 7 below shows the first five natural frequencies of the silicon wafer based the silicon material properties. From Figure 33, the time interval of the oscillatory signal measured on the oscilloscope read about 155μs, which is about 6.5 KHz. Clearly the results showed that the two frequencies are not comparable to each other. In the likelihood vibration may exists, it is of very small or negligible amount. Following that analysis, vibration is ruled out.

After several weeks trying to obtain the right thermal signal, it came to mind, that the photodiodes were in fact detecting the scattered or reflected pulse energy or intensity of the heating laser. As it turned out, the high intensity from the Nd:YLF heating laser overshadowed the signal from the probe beam detected by the silicon photodiodes.

The experimental set-up was then redesigned so that the photodiodes would be restricted to light from the probe beam only. The thin wafer is glued directly on the front side of the hardboard enclosure as opposed to being on a support, at a distance from the enclosure

hole that permits the heating laser to go through. This modification paid off as the thermal conduction profile finally took shape. However, some disturbance was still present. Figures 34 and 35 below shows the next two voltage signals obtained after the modifications on the enclosure.

After vibration causes, the other main sources could result in noises from the surroundings, or equipment devices around the experimental set-up. First thought came on the New Focus amplifier. The amplifier was then replaced at first by a locked in function generator and some disturbances were slightly eliminated. Therefore, a few improvements were made to the current system and discussed more in details in the next sub-section.

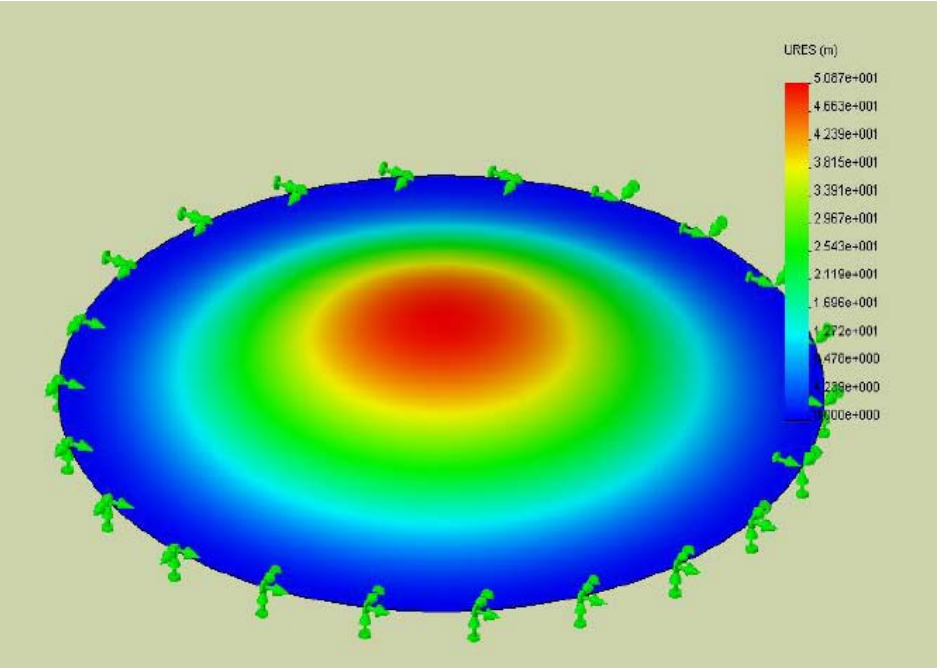

Figure 32: Vibration modal of silicon wafer

Mode List		
Frequency Number	**Hertz**	**Seconds**
1	29.405	0.034008
2	61.225	0.016333
3	61.235	0.016331
4	100.51	0.009949
5	100.57	0.0099438

Table 7: Frequency vibration mode list

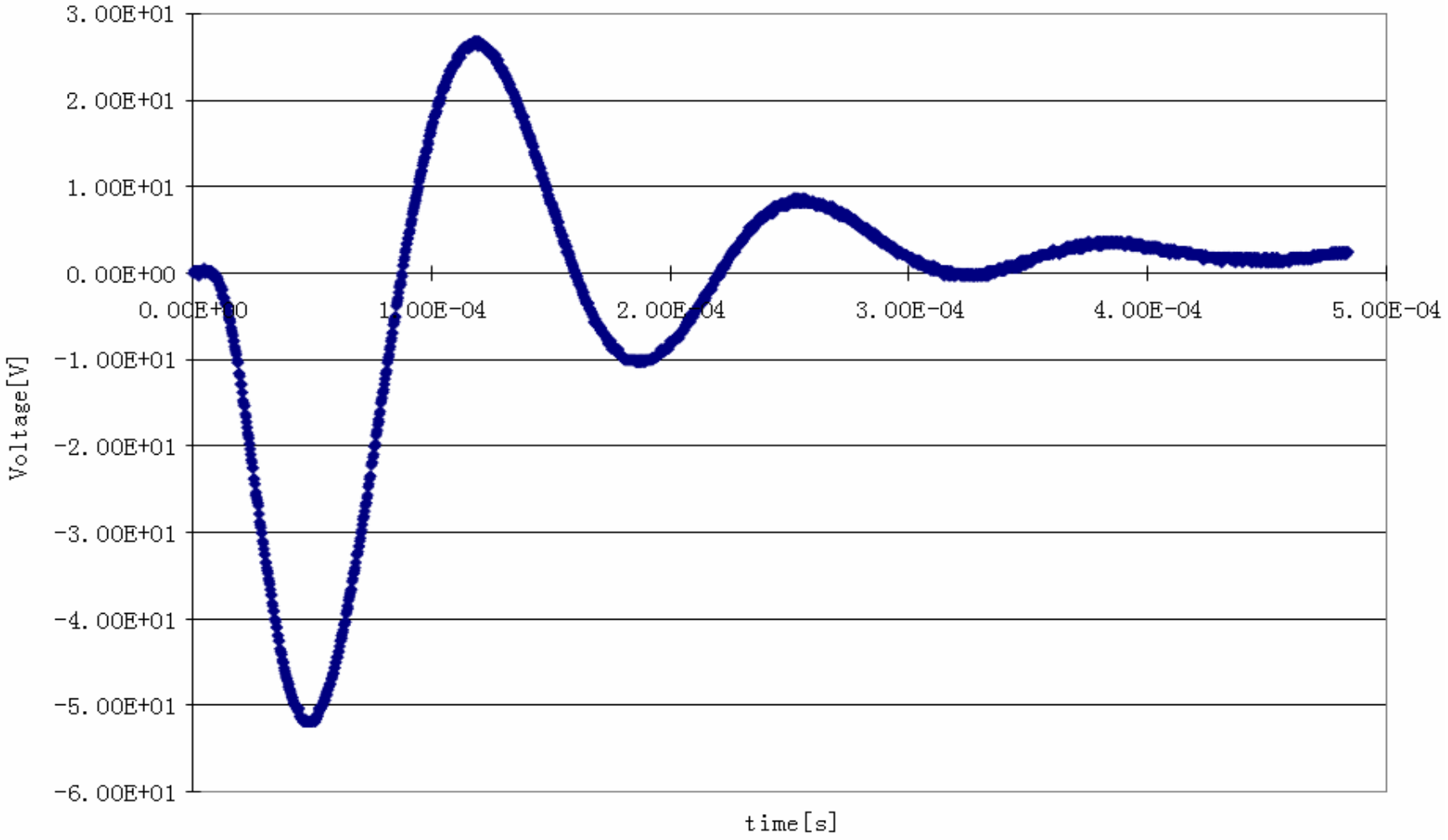

Figure 33: First result – Presence of oscillation signals of about 155µs apart; no thermal signal

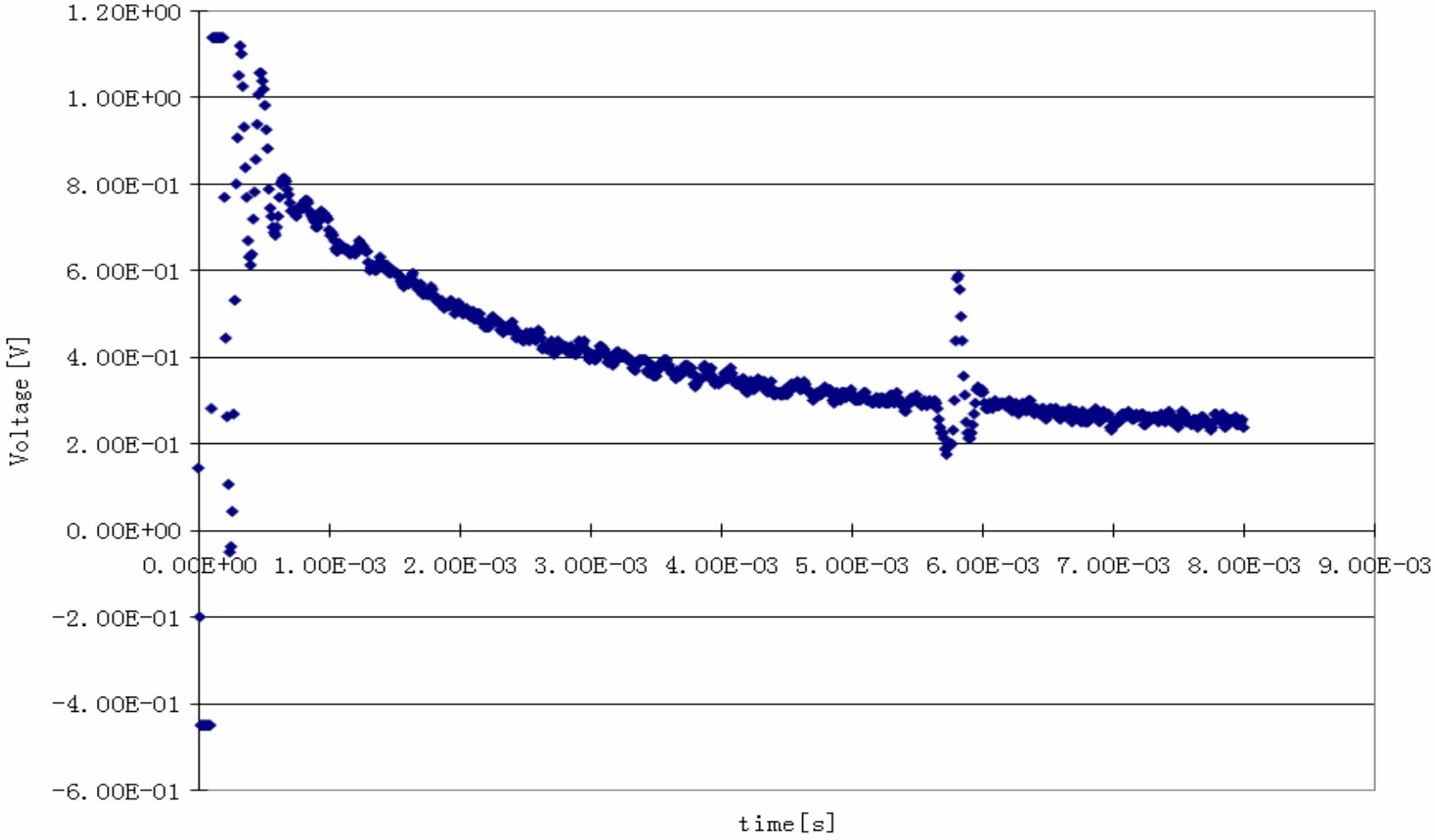

Figure 34: Second Result - Thermal profile shaping up with some oscillations at the beginning of the cooling side

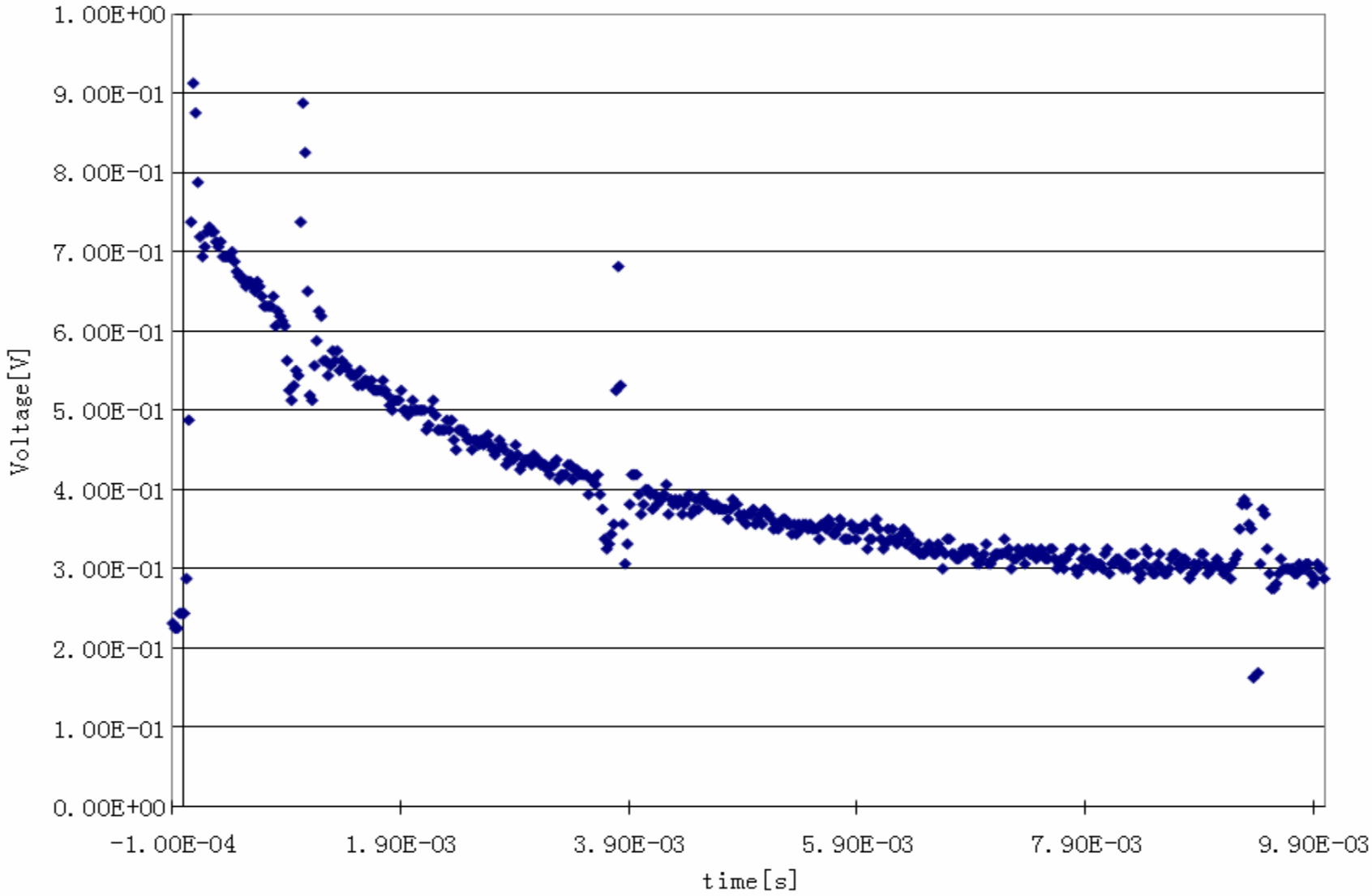

Figure 35: Third Result - Disturbance at the start of the cooling area with some repeating noise signals

5.3 Improvement in Experimental Set-up

After a few more weeks, some further improvements were made to the current set-up. Noise became one primary cause of concern in the signals, especially after vibration was ruled out and one source of noise was from the current pre-amplifier itself. Thus, a new SR 570 low-noise current pre-amplifier was purchased and replaced the New Focus amplifier. The SR 570 preamplifier is advantageous in threefold. Firstly, it provides a voltage output proportional to input current with sensitivities ranging from 1mA/V down to 1pA/V compared to 2mA/V to 200nA/V in the old one. Thus the SR 570 amplifier has a wider sensitivity, especially at the lower (smaller) ends. Secondly, the low-noise amplifier could sink current directly into a virtual null or selected DC bias voltage. The DC voltage at the input can be set as a virtual null or biased from -5V to + 5V. In this work, the setting used was in low-noise mode and the output is inverted relative to the input. This setting, with the bias, enables the whole experiment to rely on one photodiode only instead of two. This helps as it reduces noise in additional BNC cable used, but also at the junction where the reference and signal diodes meet up. Thirdly, The SR 570 operates with a fully floating ground with the amplifier ground isolated from the AC power supply. Signal inference and digital noise can be eliminated by shutting down the processor clock on the front panel.

Finally, an adjustable filter is placed in front of the signal photodiode to reduce any noise associated with the probe laser. With those changes, the final experiment set-up is reconfigured and shown in Figure 36. The gain amplifier, G, is the only difference between the two pre-amplifiers as far as the reflectivity models and calculations are concerned. The gain used is 500nA/V in the new low-noise amplifier. Using the same procedure and method

as in Chapter 4, the voltage-temperature conversion becomes **49mV** corresponding to a rise in temperature of **10**˚**C**.

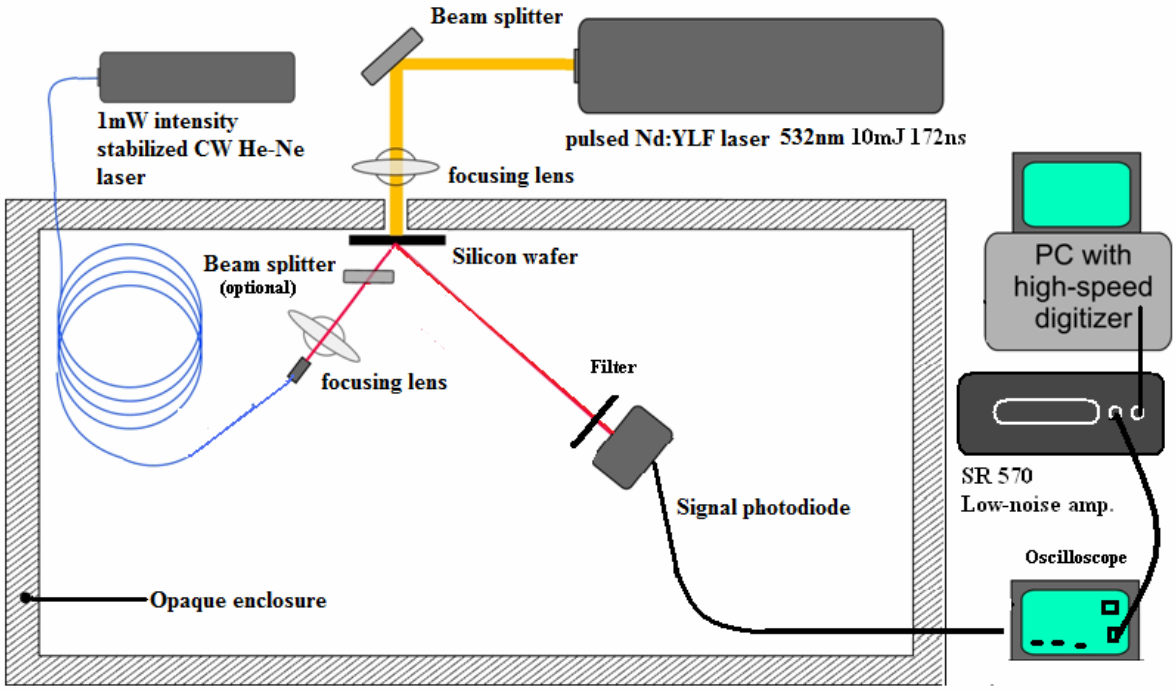

Figure 36: Final improved experimental set-up

5.4 Final Result and Discussion

Following the above improvements, the thermal signal, corresponding to the transient heat conduction through the wafer is finally obtained, and displayed in Figure 39. The corresponding change in temperature is calculated using the voltage-temperature conversion in the previous section and the temperature change is plotted versus time. The maximum transient temperature rise from the experiment is about 10.55ºC after a short time of about 76μs. The half-time, $t_{1/2}$, at 5.26ºC is 24.24μs. According to the experimental data, the rear surface of the sample cools down very quickly as well, in about 1ms. However, the half-time obtained from the thermal signal is about two times greater than what the simulation predicted earlier (Chapter 3). The temperature rise is also very significant in the simulation as opposed to the thermal signal in the experiment. Figure 40 shows a comparison between the thermal signal and the simulation.

The difference and discrepancy between the two results shows that the experimental measurement is far below that expected. The simulation, on the other hand was right because a similar model was run for a 1-D case and yielded the same results as Parker's 1-D case using his analytical solutions as discussed in Chapter 3. Thus the offset was from the experiment. As explained in the beginning of this thesis, the key to measure the temperature change with this concept is using the thermoreflectance technique. The possible source of discrepancy is the effect, shape and size of the probe laser beam and also the heating laser. The probe beam can be assumed to have a circular shape, diameter of about 0.7139mm at zero angle of incidence. However, the probe beam in the experiment is oriented at a steep angle of incidence of 70º, thus the beam changes shape as it is reflected off the wafer. In other words, the beam adopts more, or less, the shape of an ellipse as the angle of incidence

increases. Figure 37 shows the ellipse probe beam at an angle of incidence of 70º. Based on the diameter of the probe beam before reflection, the ellipse's full width is found to be 2.09mm. Since the heating beam itself is smaller compared to the probe beam (even at zero incidence), 0.6mm compared to 0.7139mm, the probe beam size becomes significantly larger when reflected at 70º. It can be seen clearly from Figure 38 how the probe beam shape in the form of ellipse (red) is compared to the heating beam (green) and the sample wafer. Thus, a few arguments on the beam sizes could be made to account for the difference in temperature between the experimental data and the simulation model: 1) the probe beam laser (which acts a detector in a way) is not capturing all the heat flux from the heating laser because of its wider dimension compared to the heating laser diameter. Figures 41 and 42, in the next section, show several rear thermal profiles from the centre of the heating laser. The temperature rise is at its maximum, obviously, at the centre (0mm), but a sudden temperature drop, almost a third, is noted right outside the heating region (profile at 0.3mm). The temperature decreases more away the centre. Since the heating beam area is too small compared to the probe's, the latter would barely be able to detect that big of a rise in temperature. The explanation is that the probe beam is detecting the heat outside the heating beam diameter. Further, Figure 43 shows a "simulation" graph, where the temperature rise at each nodes is displayed. In this graph, only six times were picked, but it can be seen that nodes within the heating area changes significantly, while those after 0.3-0.5mm barely detect any change in temperature. 2) Ideally it would be best to have the heating laser diameter much larger than 0.6mm (and the ellipse) so that the ellipse probe beam could capture all the heat flux. Unfortunately, the heating laser is already being used at its maximum energy. Using a diverging lens may increase the beam diameter but that will also

decrease its power. A much more sophisticated laser can be used but, unfortunately, that outspends the budget limit for this simple concept/work, thus the existing Nd:YLF was used. 3) As discussed earlier, the heating laser has a multi-mode pattern that could affect the output energy of the heating beam, depending on the location of the high or low intensity or "distribution". It is not known and difficult to tell which part exactly inside the beam is that pattern, or whether when the heating pulse strikes the wafer, it does so with the highest intensity or the low region.

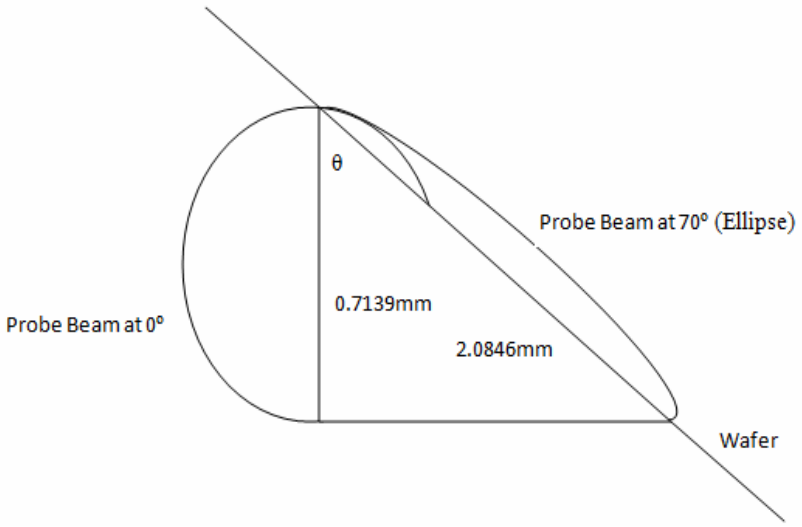

Figure 37: Width of Ellipse at θ = 70°

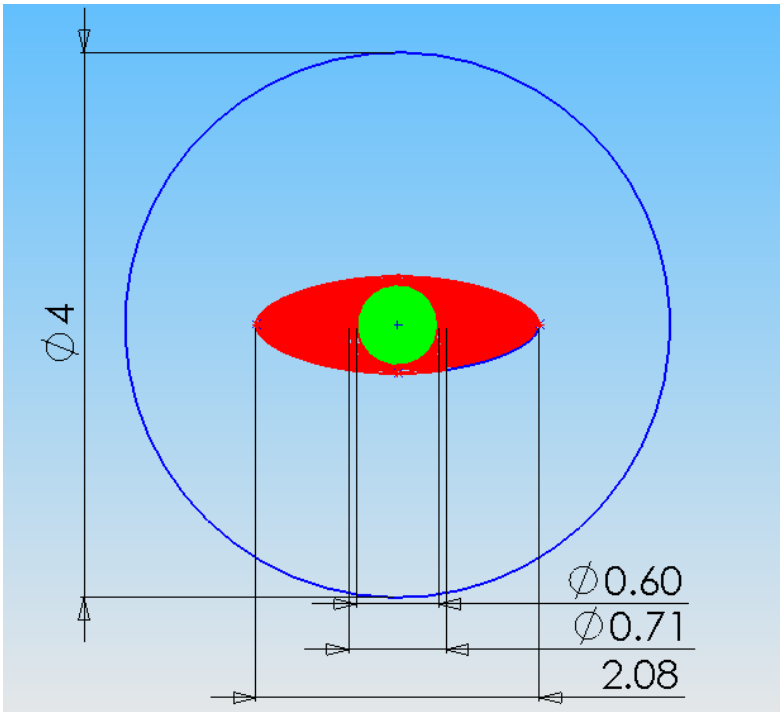

Figure 38: Probe beam shape (red) compared to the heating laser (green) on sample wafer

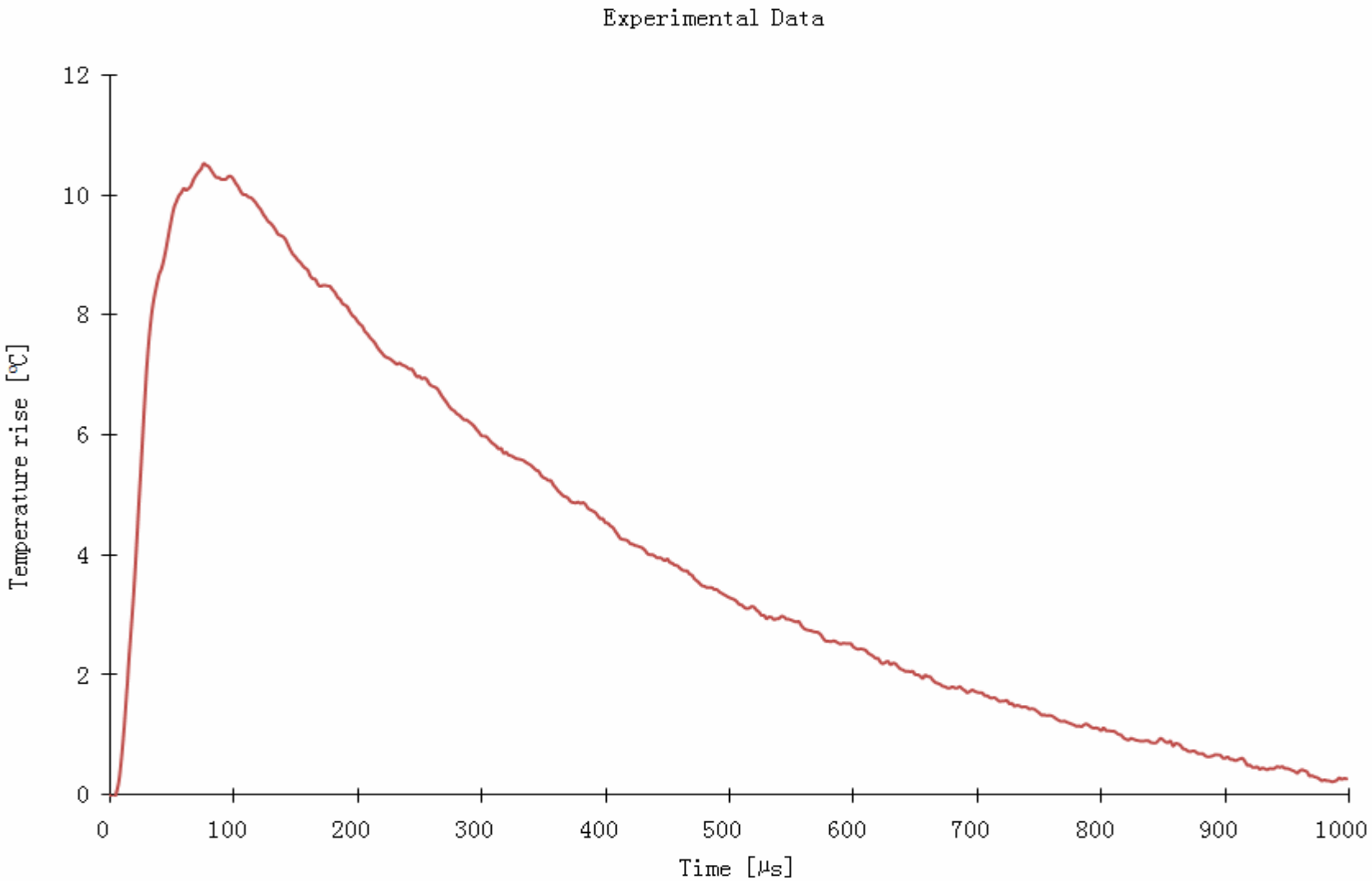

Figure 39: Final Result – Thermal Signal

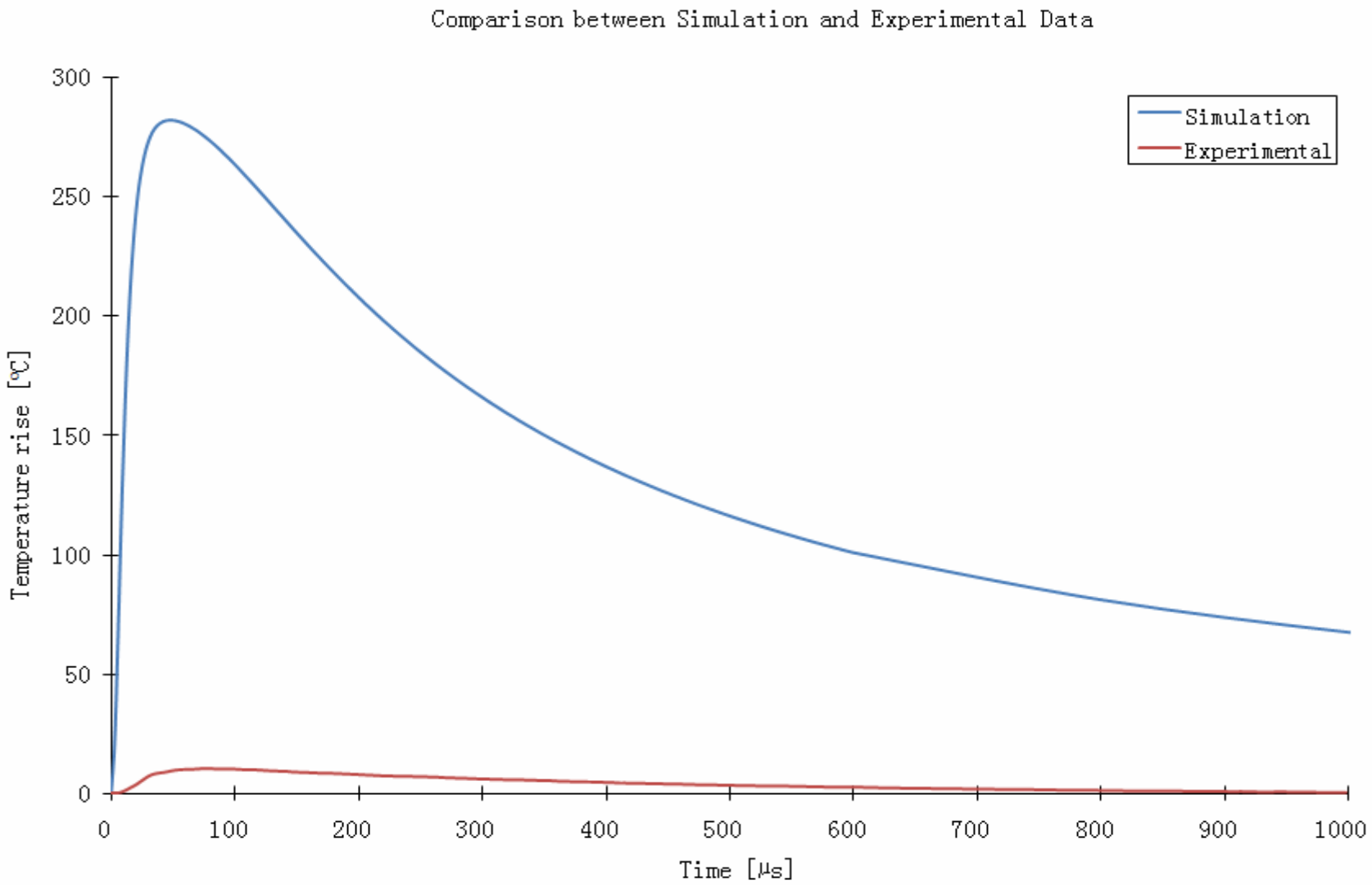

Figure 40: Experimental results compared to Model Simulation

5.5 Determining α and k

Once the final result is obtained and data collected, the final result is used as a reference to find the thermal conductivity and diffusivity of the wafer. A search of the thermal conductivity of silicon that yields a closer agreement, or close match, to the experimental data is made. The selected thermal property is then substituted in the model in ANSYS for re-runs until the best agreement is seen.

Because the simulation and the experimental data did not agree in terms of the maximum temperature rise, several transient thermal profiles at different locations (nodes), from the centre of the heating area, are imported and analyzed. The next few graphs show the outcome of the profiles. Figures 41 and 42 represent the transient-temperature curves for a few locations ranging from 0 to 1.1mm, beyond the length of the ellipse. An average of all curves as well as an average from nodes 0.21 to 0.39mm are made and plotted in Figure 44. The average of all the nodes represents the best estimate. The maximum temperature rise is reduced to about 90ºC but the half-time rise is about 8.25μs, which is close to the half time at the centre but still far away from the experimental value.

The next step is to substitute different values of thermal conductivity, k, in ANSYS to yield the closest half-time possible to the experiment. Different values of k will result in different transient responses that will match the experimental value of 24.24μs. After a few tries, a value of k of 53.6 W/m*K resulted in the best agreement. The maximum temperature rise, for k = 53.6 W/m*K is still very significant, about 280ºC, compared to the experiment. But at this point, it is concluded the diameter of the lasers and characteristics of the heating laser beam (diameter) made up for it. So it is left to compare the half-time of k=53.6 W/m*K and

the experimental value. After the simulation, an average curve of thermal profiles at a few nodes is made and then compared to the experimental data.

A normalization of the temperature rise for both the experimental results and for the simulation of k= 53.6 (and indeed) 140 W/m*k is determined, and displayed in Figure 45. It can be seen that the half-time of the simulation and experimental values are close. The half-time in the new simulation is about 25.17 μs.

The whole idea for choosing a thermal conductivity value of 140 W/m*K at the beginning (Chapter 3), is because that value was described in various references for silicon in general (or undoped-silicon or pure silicon). At first the result still shows a big difference of 140 against 53.6, but it is later found out that silicon wafers and their thermal conductivities depended heavily on their types and also their orientations. Srinivasan, Jayachandran *et al*. [33] did some investigations on doped-silicon in different orientations. Their values were ranging from 40-45 W/m*K for n-Silicon types and 37-43 W/m*K for p-Si types. Table 8 shows the thermal properties of n-type and p-type silicon and the results from this work.

At the end, it may turn out the true value from this concept (53.6 W/m*K) is the good one based on the assumption the sample wafer is indeed doped and disregarding the temperature difference. However, this cannot be truly answered because the sample, or tested, silicon doping types and orientations are not known.

It all means that the initial thermal conductivity in the model (140), which was thought to be the right value for the wafer, can in fact be considered a random guess until the true value of about 53.6 W/m*K is obtained.

Thus, using equation (3-3), the thermal diffusivity can be calculated to be $0.35*10^{-4}$ m^2/s.

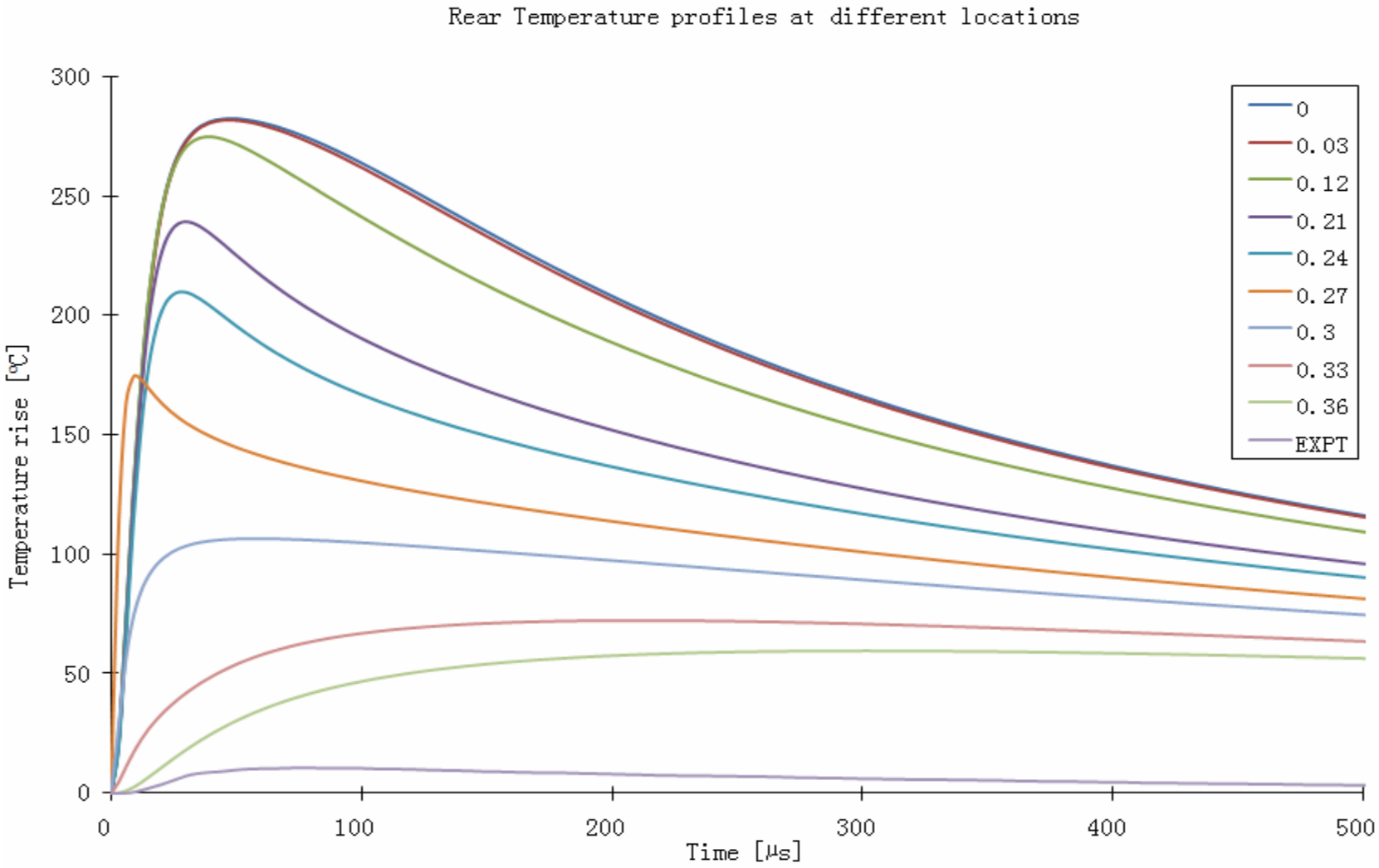

Figure 41: Rear Temperatures at different locations from 0 to 0.36mm

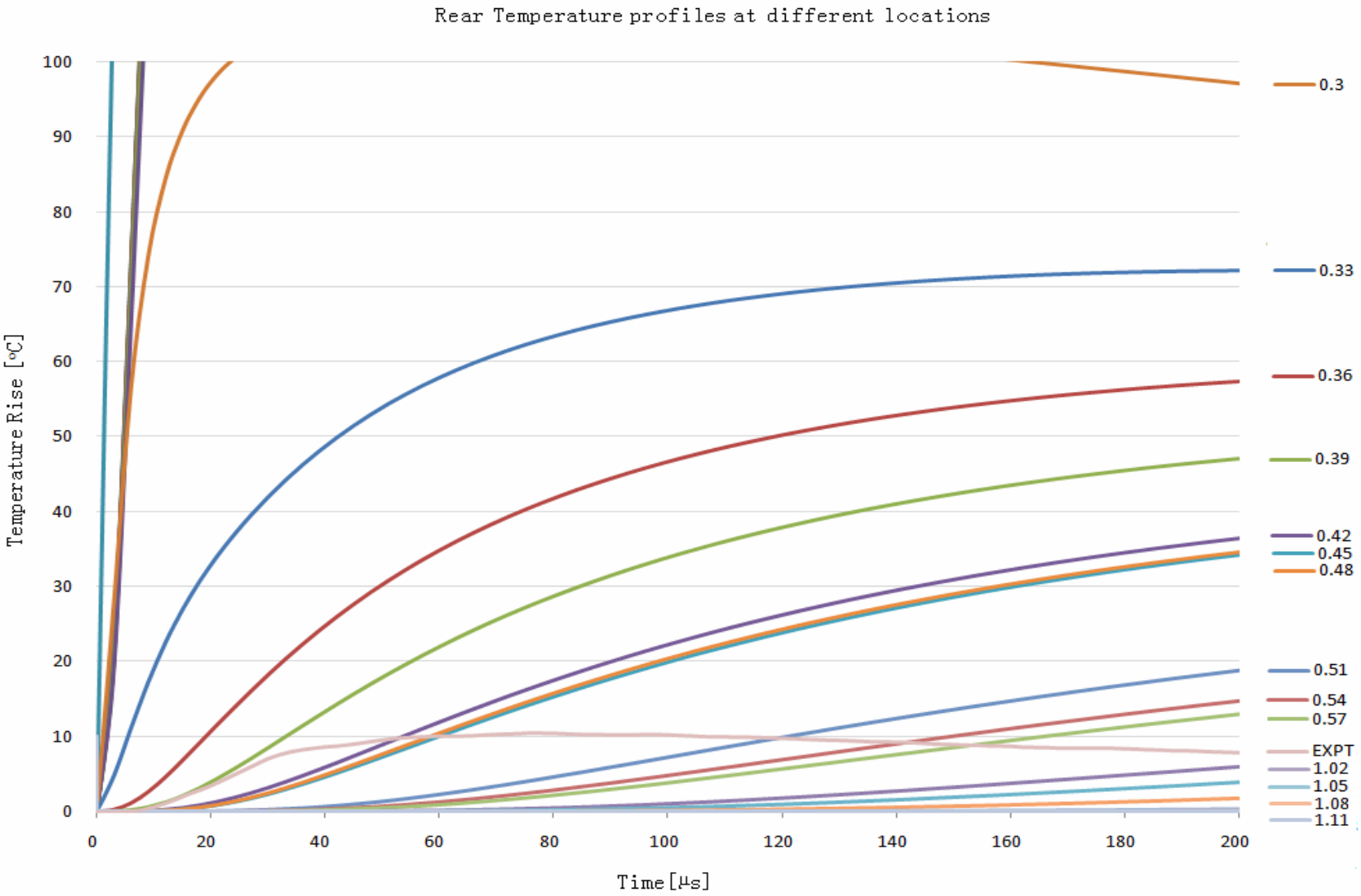

Figure 42: Rear Temperatures at different locations up to 1.11mm

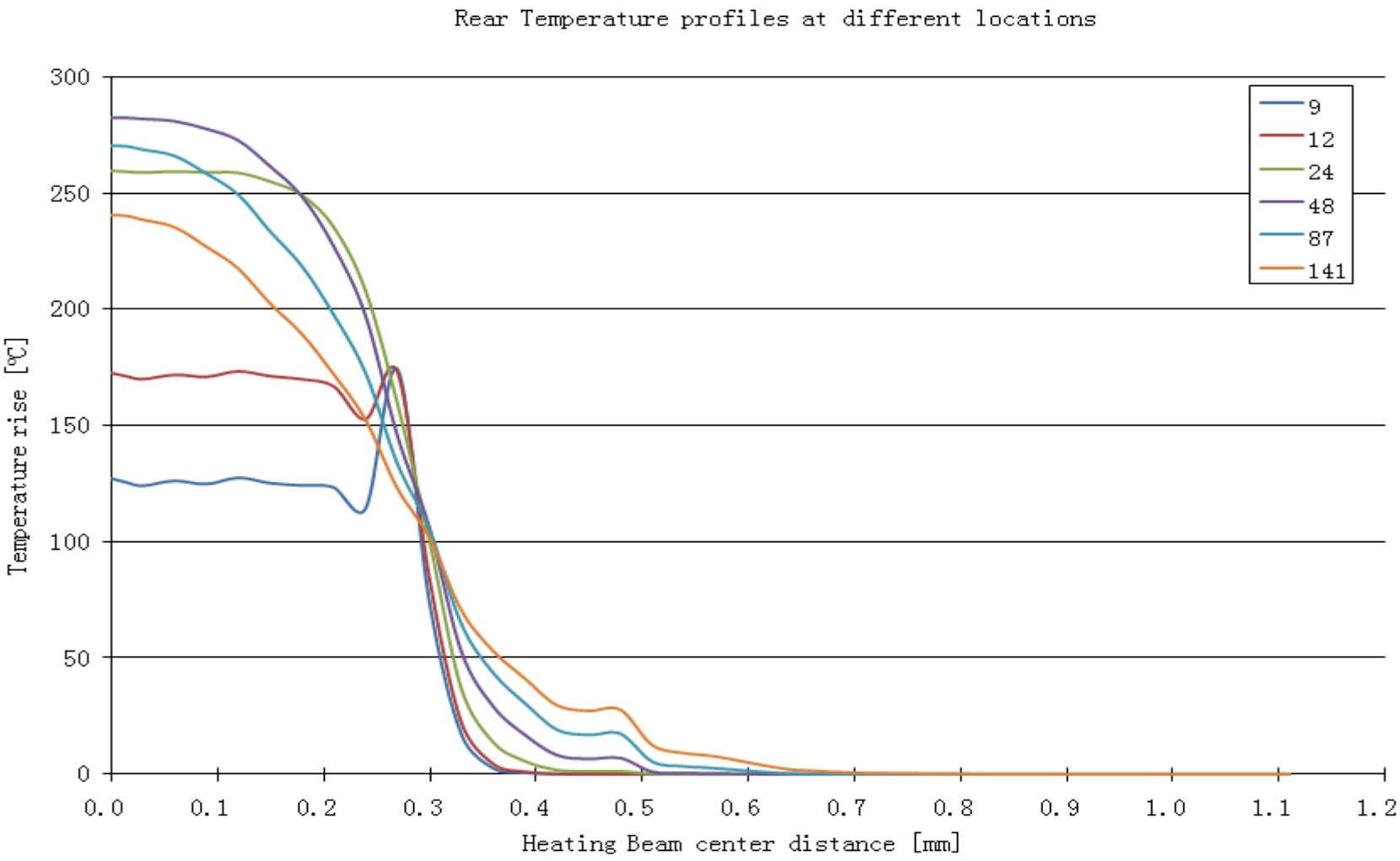

Figure 43: Maximum temperature rise at each nodes for six different times

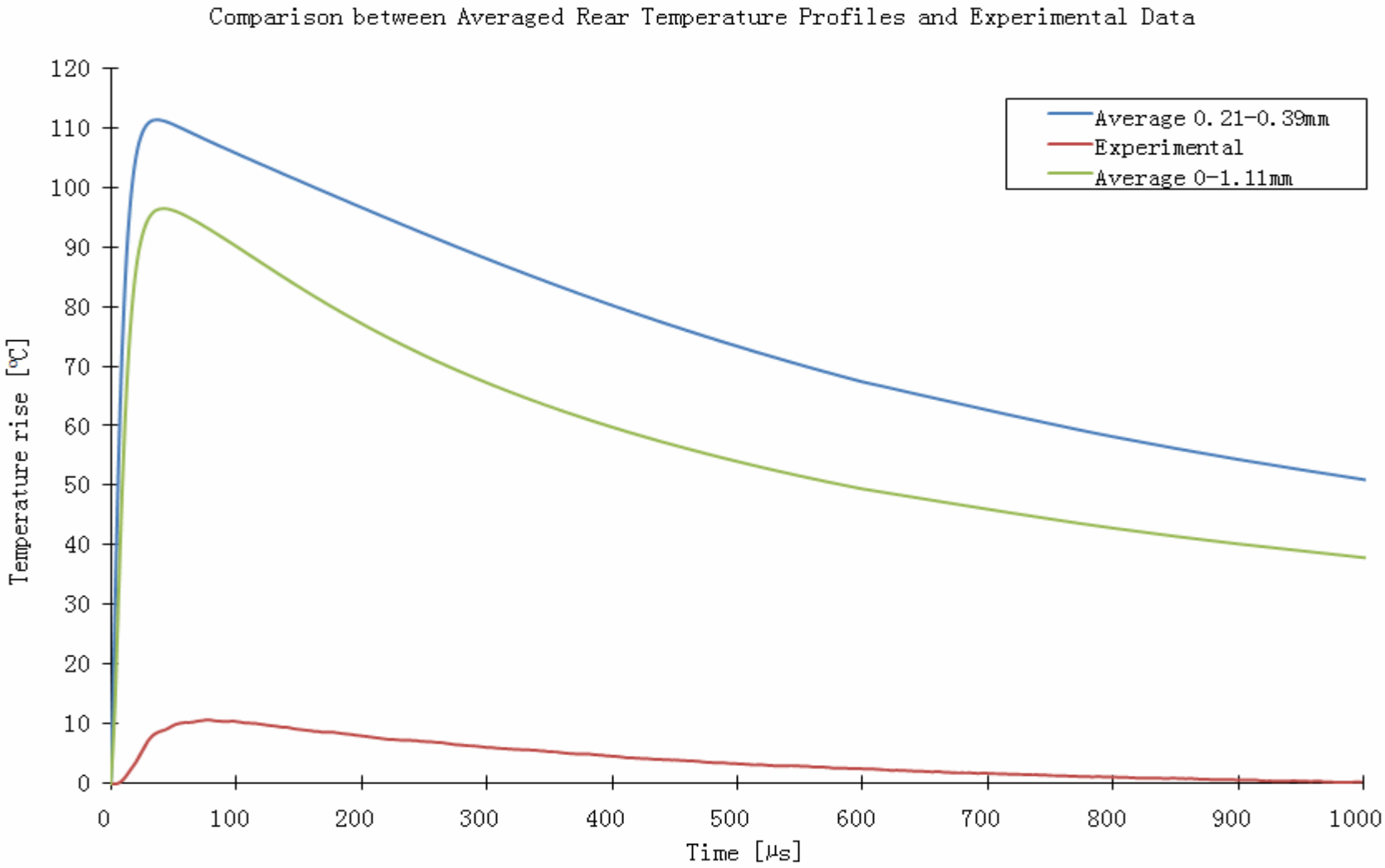

Figure 44: Average Rear Temperature Profile compared to experiment

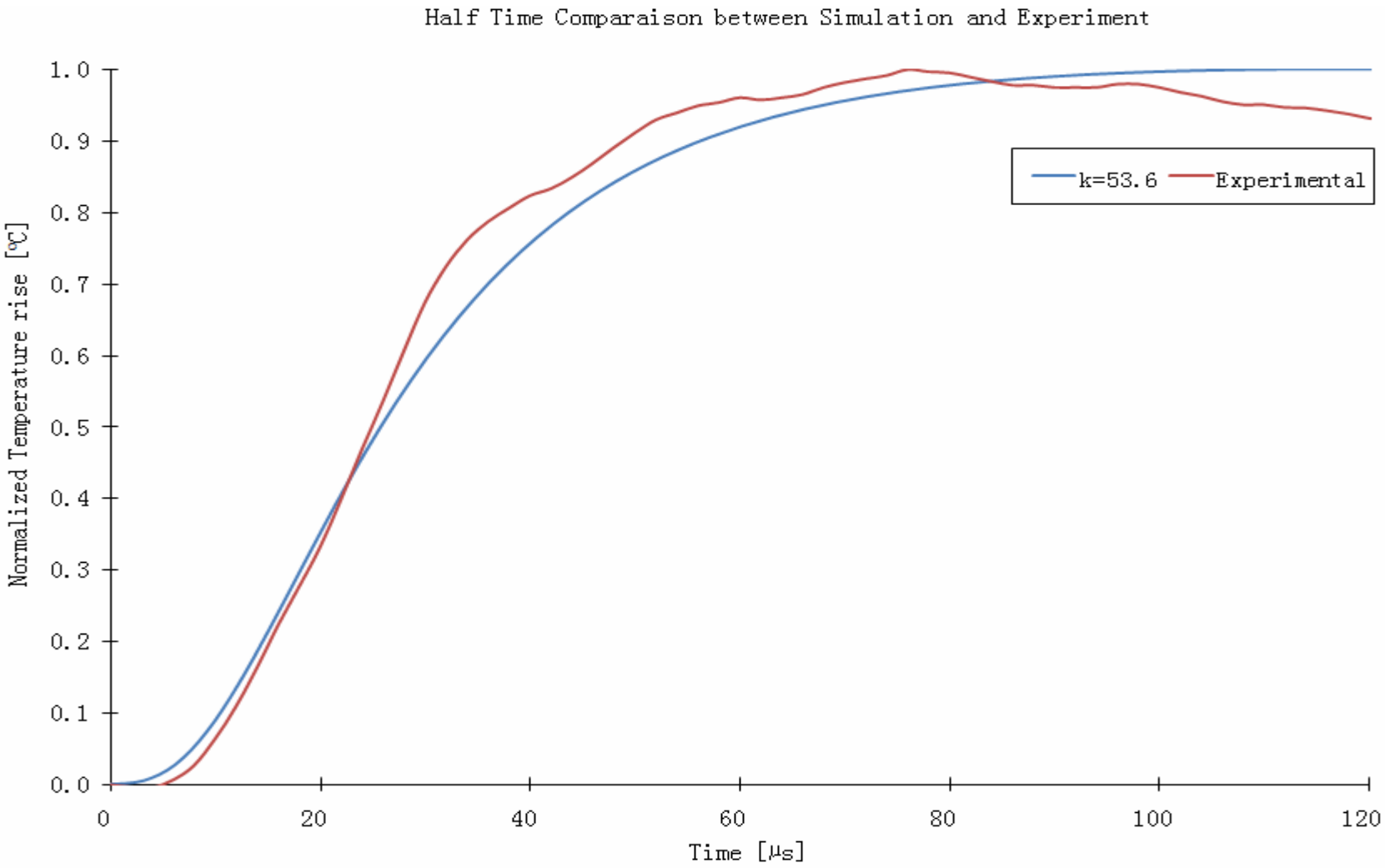

Figure 45: Comparison of half-times for simulation k=53.6 W/m.K and experiment

5.6 Uncertainty Analysis

Experimental results are subjected to two general types of errors, namely measurement errors and non-measurement errors [26]. The former are associated with uncertainties that exist in measured qualities contained in the equation used to compute the diffusivity and conductivity from experimental data. Non-measurement errors are usually associated with deviations of actual experimental conditions.

In this work, measurement errors include errors associated with determining the maximum temperature rise from the experiment (which results from the reflectivity models; the accuracy of the angle of incidence of the probe beam and errors associated with the photodiodes response and the low-noise amplifier). Other sources also include the thickness of the wafer and the laser beam diameters.

The major sources of non-measurement errors are 1) finite pulse effect, (2) heat losses, (3) non-uniform heating, and 4) in-depth absorption of the pulse energy. It should be noted that these effects are not properly classified as errors but merely deviations from the ideal situation in which these effects are assumed to be negligible. It is entirely feasible to propose models which incorporate these effects and to generate mathematical expressions which properly account for them. Problems arise, however, in mathematically expressing the actual experimental conditions present, e.g., in knowing quantitatively exact heat loss from each surface.

Although the silicon thermal properties are measured in this work, the change in temperature, ΔT , which is based on the measurements of several parameters, is the final quantity of interest. Using the root-sum- square method (Figliola and Beasley, 1995), the total uncertainties concerning the measurement of ΔT can be expressed as:

$$U_{\Delta T} = \pm\sqrt{\sum_{i=1}^{N}\left(\frac{\partial \Delta T}{\partial x_i}U_{x_i}\right)^2} \tag{5–2}$$

where $U_{\Delta T}$ is the total uncertainty in ΔT , U_{x_i} is the uncertainty of parameter x_i, $\partial V/\partial x_i$ is the sensitivity of ΔT to x_i, and N is the total number of error sources, respectively. Therefore, the uncertainty analysis is processed by finding the total uncertainty $U_{\Delta T}$, which is estimated by analyzing each error source. In order to estimate $U_{\Delta T}$, dominate parameters that are important to determine ΔT are used. They are the probe beam intensity, I_I , the change in the beam reflectivity, $\Delta\rho$, the pre-amplifier gain, G, and the responsivity, R, of the photodiodes. The probe beam intensity, which depends on the resolution of the powermeter is about $\pm$ 1μW. The uncertainty of the preamplifier gain and error in the responsivity were obtained from their manufacturer's literature and found to be 0.5% and $\pm$ 0.025A/W respectively.

The uncertainty in the reflectivity is the most complicated and troublesome one. Because that parameter is a measure of the optical properties of silicon, n and k, (which themselves depend on temperature as discussed in Chapter 3 and 4) and also the angle of incidence, θ, the errors of each of these sub parameters need to be determined.

Figure 45 shows an uncertainty tree schematic [27] that can used to determine the uncertainty in ΔT . Applying Eq. (5-2),

Level 1:

$$U_{\Delta T} = \sqrt{(\frac{\partial \Delta T}{\partial \Delta\rho}.U_{\Delta\rho})^2 + (\frac{\partial \Delta T}{\partial \Delta V}.U_{\Delta V})^2 + (\frac{\partial \Delta T}{\partial \Delta I}.U_{\Delta I_I})^2 + (\frac{\partial \Delta T}{\partial \Delta G}.U_{\Delta G})^2 + (\frac{\partial \Delta T}{\partial \Delta R}.U_{\Delta R})^2}$$

Level 2:

$$U_{\Delta\rho} = \sqrt{\left(\frac{\partial\Delta\rho}{\partial\Delta\frac{d\rho}{dn}}.U_{\Delta\frac{d\rho}{dn}}\right)^2 + \left(\frac{\partial\Delta\rho}{\partial\Delta\frac{dn}{dT}}.U_{\Delta\frac{dn}{dT}}\right)^2} + \sqrt{\left(\frac{\partial\Delta\rho}{\partial\Delta\frac{d\rho}{dk}}.U_{\Delta\frac{d\rho}{dk}}\right)^2 + \left(\frac{\partial\Delta\rho}{\partial\Delta\frac{dk}{dT}}.U_{\Delta\frac{dk}{dT}}\right)^2}$$

the uncertainty in ΔT can be estimated. However, the uncertainty in $\Delta\rho$ is too difficult to be determined as it depends on so many parameters, (dependant on ΔT themselves). Level 2 above was difficult to be determined. Thus the uncertainty in this work is estimated based on the reflectivity models directly rather than using Eq. (5-1). The change in temperature was computed from the voltage readings (Labview or Oscilloscope) using the temperature-voltage conversion (Chapter 4 and 5). But as mentioned earlier, the experimental results had an error of 4% compared to values from the reflectivity model (from validation of model in preliminary work). ΔT may be estimated to have an error of 4% from the voltage reading.

Uncertainties resulting from the pulse energy, heating laser diameter and wafer thickness could be also be classified as measured uncertainties but they are not directly involved in finding the change in temperature.

Each pulse energy has an uncertainty which comes from the measured value of a single pulse's peak voltage at different frequencies and the reflectivity of the heating laser beam as discussed in Chapter 4. The latter is depends on the powermeter resolution again. The pulse duration also has some uncertainties as it was assumed the pulse shape earlier is uniform.

The heating beam diameter, on the alignment paper, is practically measured using an electronic caliper. The measured value is 0.6 ± 0.1mm, resolution of the caliper, while the wafer thickness error is from the resolution of the dial is about 0.6%

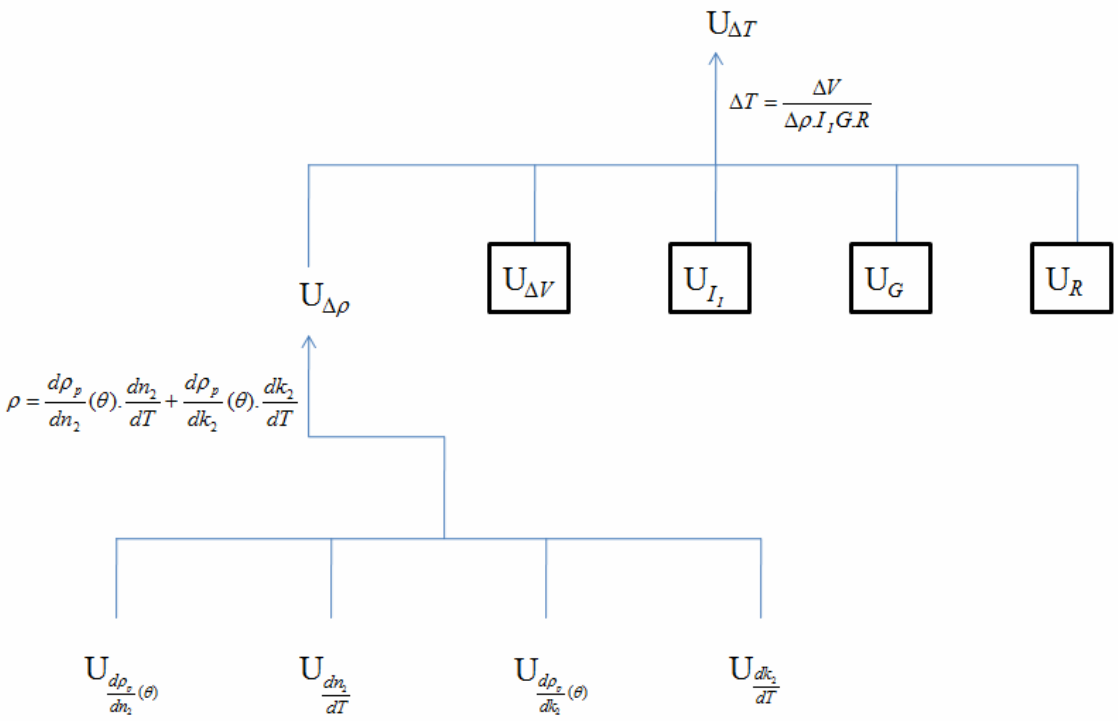

Figure 46: Uncertainty tree for ΔT

Finally, to summarize the results from this work, a table shows the comparison of the thermal properties of the sample wafer as follows:

Silicon wafer	Literature	Measured
k [W/m*K]	n-Si(111) 45.0[1] n-Si(100) 40.0[1] p-Si(111) 43.0[1] p-Si(100) 37.0[1]	53.6 (simulation)
α [*10^{-4} m^2/s]	n-Si(111) 0.28[1] n-Si(100) 0.25[1] p-Si(111) 0.26[1] p-Si(100) 0.23[1]	0.35 (simulation)

[1]Srinivasan et al.[33]

Table 8: Summary of results

6. Concluding Remarks

This work presents the concept of a spatially-resolved laser-based instrument to measure the thermal conductivity and thermal diffusivity of a silicon wafer. The experimental principle is based on the thermoreflectance method, and the experimental set-up is small, inexpensive and reliable. The thermal conductivity and diffusivity (transient-response time) appear comparable to literature, considering the tested wafer is doped and of known orientation. However, the temperature rise was significantly larger in the model but the experiment could further be improved, especially with both laser beams and their characteristics (power etc.). As an added feature, the temperature dependence of the silicon wafer refractive index, $\frac{dn}{dT}$, and extinction coefficient, $\frac{dk}{dT}$, are also determined. Alternatively, this concept can potentially be used to measure the thermal conductivity, thermal diffusivity and the temperature refractive index of other solids and thin films.

6.1 Conclusion of Present Work

The experimental set-up, which is custom-designed and built for the present work is described and outlined in Chapter 2. The 4mm-diameter wafer is glued directly on the hardboard enclosure. A Nd:YLF laser system serves as the heating source. The heating laser pulse is powered on by a controller box but triggered by the data acquisition card, or by a function generator. The reflectivity change of the probe beam laser is captured by one single

signal photodiode with the output photocurrent converted into a voltage signal by a low-noise preamplifier. Finally the experimental data is collected using a data acquisition card, or by an oscilloscope.

Physical Models for heat conduction and the probe beam reflectivity are presented in Chapter 3, with governing equations, boundary and initial conditions for the wafer. The equations are solved using a numerical finite element simulation package in the form of ANSYS. The transient temperature change in the model is then compared with the experimental data to find the thermal conductivity and thermal diffusivity of the wafer.

In Chapter 4, a series of important experimental issues are addressed. These include verifications of the heating laser pulse energy, time duration and diameter; as well as thickness of the wafer. Proper alignment of the two laser beams on either side of the wafer is made, with the use of a special device called an electroviewer. More importantly, the reflectivity models/equations for both p-and s-polarized planes are compared with initial results, and a relation between voltage change and temperature change is determined.

Experimental results and discussions are presented in Chapter 5. Procedures for collecting and processing of the experimental data are discussed first. The initial results and improvements to set-up leading to final result are discussed. From the model, the thermal conductivity that yields the best agreement to the experimental data is the true measured value.

6.2 Future Research Directions

Some possibilities and suggestions for improving the present study as well as for future research directions are outlined below:

1. Further modifications in the experimental set-up

The probe beam can be focused using a lens to narrow its wide elliptical width. A more sophisticated and powerful laser that can output and much more powerful and larger beam diameter at the same time can be used.

The heating laser could be placed on the same side as the probe beam laser. That will increase the temperature rise of the back surface. The experiment could be repeated for different angle on incidence, closer to the Brewster angle. However both situations have limited capabilities. In the first case, the diodes will detect more light from the heating laser because of its high intensity compared to the probe, unless special "tubing" or some sort is built to encase the probe beam's path. In case two, experimentally, it is more and more difficult to get the best angle of incidence especially nearer to the Brewster angle, but it would be interesting to see how much a change there is in the reflectivity and hence temperature change.

It would be better to have a radiation detector attached close to the wafer to have a reference measurement, to compare the temperature change from the present concept.

2. Finding the in-plane thermal conductivity and finding the spatial resolution

The advantage of the spatially-resolved method is to be able to measure the in-plane thermal conductivity. Because of time constraints, it has not been tested yet. The spatial resolution can also be determined.

3. Multiple Heating Pulse Improvement

At present, only a single thermal pulse is used to produce the temperature gradient in the wafer and thus the time-dependant temperature change. If the wafer is heated by a pulse train with a certain pulse frequency, more features will be obtained from the probe beam

reflectivity (Figure 46). This may provide more information for the numerical model to search for the target values of the wafer thermophysical properties.

4. Laser-based Thermal Pulse Measurement of Solid Thermal Conductivity and Thermal Diffusivity

Measuring other solid coatings and thin films. As discussed in Chapter 1, the thermal conductivity and thermal diffusivity are very important thermophysical properties for solid coatings and thin layers. Although values of these parameters for pure materials may be available from literature, it is not the case for solid layers and coatings. This instrument is a good candidate tool to practically measure the thermal conductivity and thermal diffusivity of solid layers due to the ease and simplicity. Multi-layer coatings or through thickness measurements can be made.

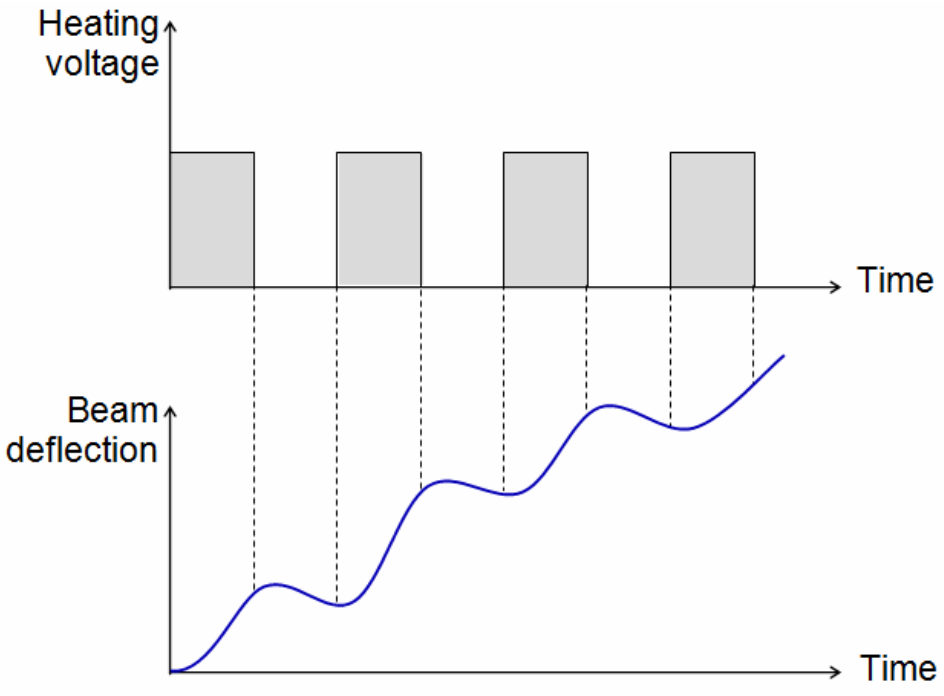

Figure 47: Beam deflection in multiple heating pulses

References

[1] R P Tye (1994), *Compendium of Thermophysical Properties Measurement Methods Vol. 2* , Eds. K. Maglic et al, Plenum Press New York, 77-97.

[2] J N Sweet, M Moss, C E Sisson, (1985), *Thermal Conductivity 18* , Eds T Ashworth, D R Smith, Plenum Press, New York, 43-59.

[3] R Brandt, G Neuer (2003) Advanced Engineering Materials 5, 52-55.

[4] H Szelagowski, R Taylor, (1998) High Temp.-High Press. 30, 343-350.

[5] T Iida, R Guthrie, (1988) The Physical Properties of Liquid Metals Clarendon Press, Oxford, 232.

[6] K G Coumou, and R P Tye, (1981) *High Temp. High Press.*, 13, 695.

[7] Y Agari, M Tanaka, and S Nagai, (1987), *Thermophysical Properties 8*, Japanese Society of Thermophysical Properties, Tokyo.

[8] S Klarsfield (1984), *Compendium of Thermophysical Properties Measurement Methods*, Eds K Maglic et al, 169—230

[9] W Pratt (1969), *Thermal Conductivity* Vol.2, ed. R P Tye, pp 301-404

[10] *Guarded Hot Plate and Heat-Flow Meter Technology*, Eds C J Shirtliffe and R P Tye (1985), ASTM STP 879, ASTM, Philadelphia

[11] J D Verschoor and Ada Wilber, (1954), *Trans Am Soc Heat Vent Engrs*, 60.

[12] C M Pelanne and C B Bradley, (1962), *Mats Res Stand*, 2, 549

[13] ASTM E1530-04, *Standard Test Method for Evaluating the Resistance to Thermal Transmission of Materials by the Guarded Heat Flow Meter Technique*, ASTM Stand. Philadelphia.

[14] L Kubicar, V Bohac, (2000), Meas Sci Tech 11, 252.

[15] L Kubicar, (1991), High Temp-High Press, 23, 40.

[16] S E Gustafsson, (1991), Rev Sci Instrum. 62, 797-804M.

[17] T Log, S E Gustafsson, Fire and Materials, 19, 43-49 (1995).

[18] U Hammerschmidt, and W Sabuga, (2000), Int J Thermophys 21, 217, and 21, 1255 –1278.

[19] W J Parker, R J Jenkins, C P Butler, and G L Abbot, (1961), J Appl Phys 32, 9, 1679

[20] K D Maglic and R E Taylor, (1992), Compendium of Thermophysical Properties Measurement Methods Vol 2, Eds K Maglic et al, Plenum Press New York, pp 281-314. Also Vol1 (1984), 299-336

[21] A Cezairliyan, T Baba, and R E Taylor, (1994), Int J Thermophys, 15, 317

[22] Xu, X. and C.P. Grigoropoulos, *High temperature radiative properties of thin polysilicon films at the Λ=0.6328 μm wavelength.* International Journal of Heat and Mass Transfer, 1993. **36**(17): p. 4163-4172.

[23] Ujihara, K., *REFLECTIVITY OF METALS AT HIGH-TEMPERATURES.* Journal of Applied Physics, 1972. **43**(5): p. 2376-&.

[24] Costescu, R.M., M.A. Wall, and D.G. Cahill, *Thermal conductance of epitaxial interfaces.* Physical Review B, 2003. **67**(5).

[25] Modest M., *Radiative Heat Transfer,* 2nd edition, 1993, New York:McGraw Hill p. 89

[26] Maglic, Cezairliyan, Peletsky, *Compendium of Thermophysical Property Measurement Methods*, 8: p. 317

[27] Longtin J., *The uncertainty tree: Reducing the uncertainty of uncertainty analysis*, Review of scientific instruments, Vol 73 No. 10 (2002)

[28] Leclercq, B., et al., *Thermal conductivity of zirconia-based ceramics for thermal barrier coating.* Materialwissenschaft Und Werkstofftechnik, 2003. **34**(4): p. 406-409.

[29] Schulz, U., et al., *Some recent trends in research and technology of advanced thermal barrier coatings.* Aerospace Science and Technology, 2003. **7**(1): p. 73-80.

[30] Sampath, S., et al., *Development of process maps for plasma spray: case study formolybdenum.* Materials Science and Engineering a-Structural Materials Properties Microstructure and Processing, 2003. **348**(1-2): p. 54-66.

[31] Coddet, C., et al., *Surface preparation and thermal spray in a single step: The PROTAL process - Example of application for an aluminum-base substrate.* Journal of Thermal Spray Technology, 1999. **8**(2): p. 235-242.

[32] Li, C.J. and A. Ohmori, *Relationships between the microstructure and properties of thermally sprayed deposits.* Journal of Thermal Spray Technology, 2002. **11**(3): p. 365-374.

[33] Srinivasan R., Jayachandran J. and Ramachandran K. *Photoacoustic studies on optical and thermal properties of p-type and n-type nanostructured porous silicon for (100) and (111) orientations*. Cryst.Res.Technol. 42, No 3, 266 -274 (2007)